

Mechanosensory-Based Phase Coding of Odor Identity in the Olfactory Bulb

Highlights

- Mechanosensation in olfactory sensory neurons generates sniff-coupled oscillations
- Phase coding in mitral/tufted cells distinguishes odor from mechanical signals
- Phase coding is more stable than rate coding across time and odor concentrations
- The loss of mechanosensory-based oscillations impairs robust phase coding of odors

Authors

Ryo Iwata, Hiroshi Kiyonari,
Takeshi Imai

Correspondence

t-imai@med.kyushu-u.ac.jp

In Brief

Iwata et al. demonstrate that phase coding, but not rate coding, in mitral cells is useful for concentration-invariant odor identity coding. They also found that mechanosensation in olfactory sensory neurons facilitates, rather than masks, the robust phase coding of odors.

Mechanosensory-Based Phase Coding of Odor Identity in the Olfactory Bulb

Ryo Iwata,¹ Hiroshi Kiyonari,² and Takeshi Imai^{1,3,4,5,6,*}

¹Laboratory for Sensory Circuit Formation, RIKEN Center for Developmental Biology, Kobe 650-0047, Japan

²Animal Resource Development Unit and Genetic Engineering Team, RIKEN Center for Life Science Technologies, Kobe 650-0047, Japan

³PRESTO, Japan Science and Technology Agency (JST), Saitama 332-0012, Japan

⁴Graduate School of Biostudies, Kyoto University, Kyoto 606-8501, Japan

⁵Graduate School of Medical Sciences, Kyushu University, Fukuoka 812-8582, Japan

⁶Lead Contact

*Correspondence: t-imai@med.kyushu-u.ac.jp

<https://doi.org/10.1016/j.neuron.2017.11.008>

SUMMARY

Mitral and tufted (M/T) cells in the olfactory bulb produce rich temporal patterns of activity in response to different odors. However, it remains unknown how these temporal patterns are generated and how they are utilized in olfaction. Here we show that temporal patterning effectively discriminates between the two sensory modalities detected by olfactory sensory neurons (OSNs): odor and airflow-driven mechanical signals. Sniff-induced mechanosensation generates glomerulus-specific oscillatory activity in M/T cells, whose phase was invariant across airflow speed. In contrast, odor stimulation caused phase shifts (phase coding). We also found that odor-evoked phase shifts are concentration invariant and stable across multiple sniff cycles, contrary to the labile nature of rate coding. The loss of oscillatory mechanosensation impaired the precision and stability of phase coding, demonstrating its role in olfaction. We propose that phase, not rate, coding is a robust encoding strategy of odor identity and is ensured by airflow-induced mechanosensation in OSNs.

INTRODUCTION

Sensory systems have the ability to recognize specific features from noisy and fluctuating background signals in the external world. A central question in sensory systems is how they can quickly and reliably extract specific sensory features from such dynamic stimuli. In recent years, there has been a growing appreciation of the fact that sensory signals are represented not only by the changes of neuronal firing rate (rate coding), but also by altering the temporal pattern of firing (temporal coding) in neurons. These include changes in spike latency, oscillation phase, and interspike intervals (Buzsáki and Draguhn, 2004; Kleinfeld et al., 2014; Panzeri et al., 2010). However, the roles of these temporal patterns in sensory information processing are not fully established.

In rodents, odorants are detected by ~1,000 types of olfactory sensory neurons (OSNs), each expressing a single type of odorant receptor (OR). OSNs expressing the same type of OR converge their axons to a pair of glomeruli out of ~2,000 in the olfactory bulb (OB). Thus, odor information is spatially represented in the glomerular layer of the OB. A glomerulus is composed of excitatory mitral/tufted cells (M/T cells; 20–50/glomerulus) and inter- and intra-glomerular interneurons (Imai, 2014; Wilson and Mainen, 2006). Odors are delivered to OSNs in the olfactory epithelium (OE) via respiratory airflow, or “sniffing” for active odor sampling. As trained rodents can recognize an odor within a single sniff, it has been proposed that the activation pattern within this timescale carries sufficient information about an odor (Uchida and Mainen, 2003). It has been known that odor stimuli not only changes firing rates, but also produces odor-specific temporal spike patterns in M/T cells (Bathellier et al., 2008; Cury and Uchida, 2010; Friedrich, 2013; Hopfield, 1995; Laurent, 2002; Macrides and Chorover, 1972; Margrie and Schaefer, 2003; Shusterman et al., 2011; Spors and Grinvald, 2002; Uchida et al., 2014; Wilson and Mainen, 2006). Recent optogenetic experiments demonstrated that the mouse olfactory system can recognize the timing of inputs within a sniff cycle (Smear et al., 2011, 2013). It is also suggested that the temporal patterns in M/T cells are decoded in the olfactory cortex (Haddad et al., 2013). However, it remains unclear how odor information is encoded within fine temporal patterns and how this is beneficial for olfaction. In the present study, we examined the role of temporal coding, or more specifically “phase” coding, in M/T cells and found that phase coding is concentration invariant and allows for a stable odor coding strategy under fluctuations. We also found that airflow-induced mechanosensation in OSNs facilitates, rather than masks, the robust phase coding of odors, revealing a previously unappreciated role of mechanosensation in olfaction.

RESULTS

Olfactory Sensory Neurons Respond to Mechanical Stimuli Produced by Nasal Airflow *In Vivo*

Recent studies using isolated OE demonstrated that mouse OSNs respond not only to odorants, but also to mechanical stimuli, such as pressure-ejected saline solution or deodorized air,

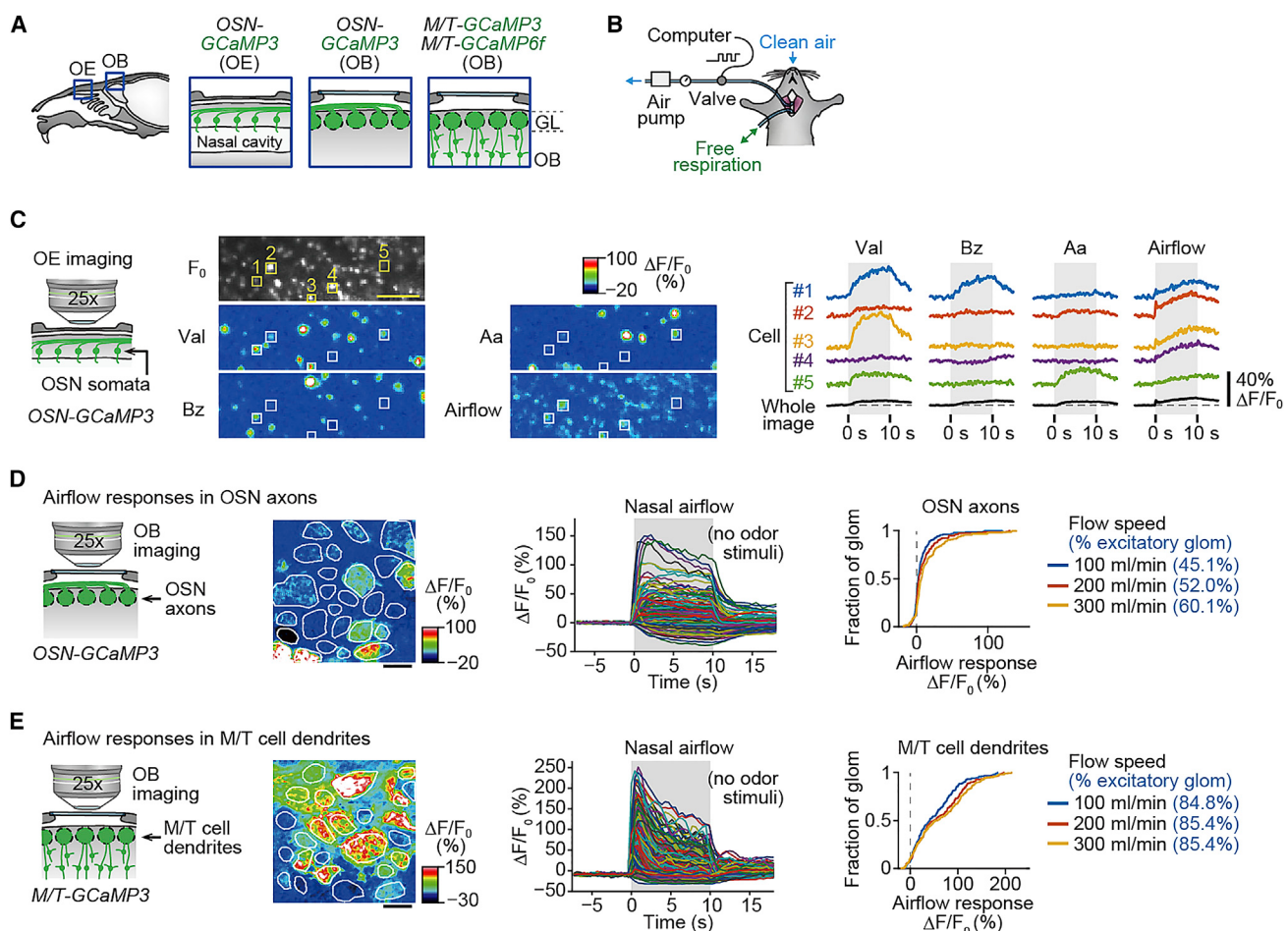


Figure 1. Airflow-Driven Mechanosensation in OSNs and M/T Cells In Vivo, Demonstrated by Calcium Imaging

(A) *In vivo* two-photon calcium imaging of the OE (OSN somata) and the glomerular layer (GL) in the OB (OSN axon terminals and M/T cell dendrites). (B) Schematic of artificial sniffing in tracheotomized mice. Airflow was generated by an air-suction pump. The timing of airflow generation was controlled by the opening of an electromagnetic valve. This setup was used for all the experiments except Figure 3. (C) Sparse responses of OSN somata to an odor (Val, valeraldehyde; Bz, benzaldehyde; Aa, amylacetate; diluted at 1:1,000) and widespread mechanosensory responses to artificial nasal airflow (an anesthetized OSN-GCaMP3 mouse). Odors were delivered to the OE for 10 s (shown in gray) in a freely breathing condition, whereas pulsed airflow (250 ms on/250 ms off) was artificially delivered for 10 s (gray) using a tracheotomized condition (flow rate 200 mL/min) of the same animal. (D and E) Responses to nasal airflow were widespread in OSN axon terminals (D; n = 173 glomeruli from n = 3 tracheotomized OSN-GCaMP3 mice) and M/T cell dendrites (E; n = 178 glomeruli from n = 4 tracheotomized M/T-GCaMP3 mice). Response heatmaps and response traces (average across four trials) were obtained at a flow rate of 300 mL/min. Pulsed airflow (250 ms on/250 ms off) was artificially delivered for 10 s (gray). Cumulative frequency plots of response amplitude are shown on the right. The fraction of glomeruli showing excitatory responses (one-tailed t test, p < 0.01) shown in the parentheses became higher as flow rate increased.

Scale bars, 100 μ m. See also Figure S1 for expression patterns of GCaMPs in the mouse lines used for imaging.

through the canonical olfactory transduction cascade (Chen et al., 2012; Connelly et al., 2015; Grosmaire et al., 2007). Thus, it has been proposed that OSNs are dual modal sensors, detecting both odor and mechanical stimuli. However, it remains unknown whether and how the olfactory system distinguishes between the two sensory modalities detected by the same OSNs.

To observe how mechanical signals are detected in the OE and transduced in the OB in more physiological conditions *in vivo*, we performed two-photon calcium imaging using genetically encoded calcium indicators, GCaMP3 or GCaMP6f (Figures 1A and S1) (Chen et al., 2013; Tian et al., 2009). To detect

mechanosensory responses in OSNs, we generated *OMP-tTA;TRE-GCaMP3* compound heterozygous mice, in which GCaMP3 is specifically and highly expressed in OSNs (OSN-GCaMP3 hereafter; Figure S1C). We used an artificial sniffing system in anesthetized and tracheotomized mice to control the nasal airflow in a reproducible manner (Figure 1B). Artificial sniffing was generated through the trachea at ~2 Hz (250 or 300 ms ON/OFF cycles, 200 mL/min), which was within the range of the resting state in awake animals (Kepecs et al., 2007; Oka et al., 2009; Verhagen et al., 2007). Deodorized clean air (passed through activated charcoal) was delivered to the nostril. To directly observe the responses in OSN somata, we made an

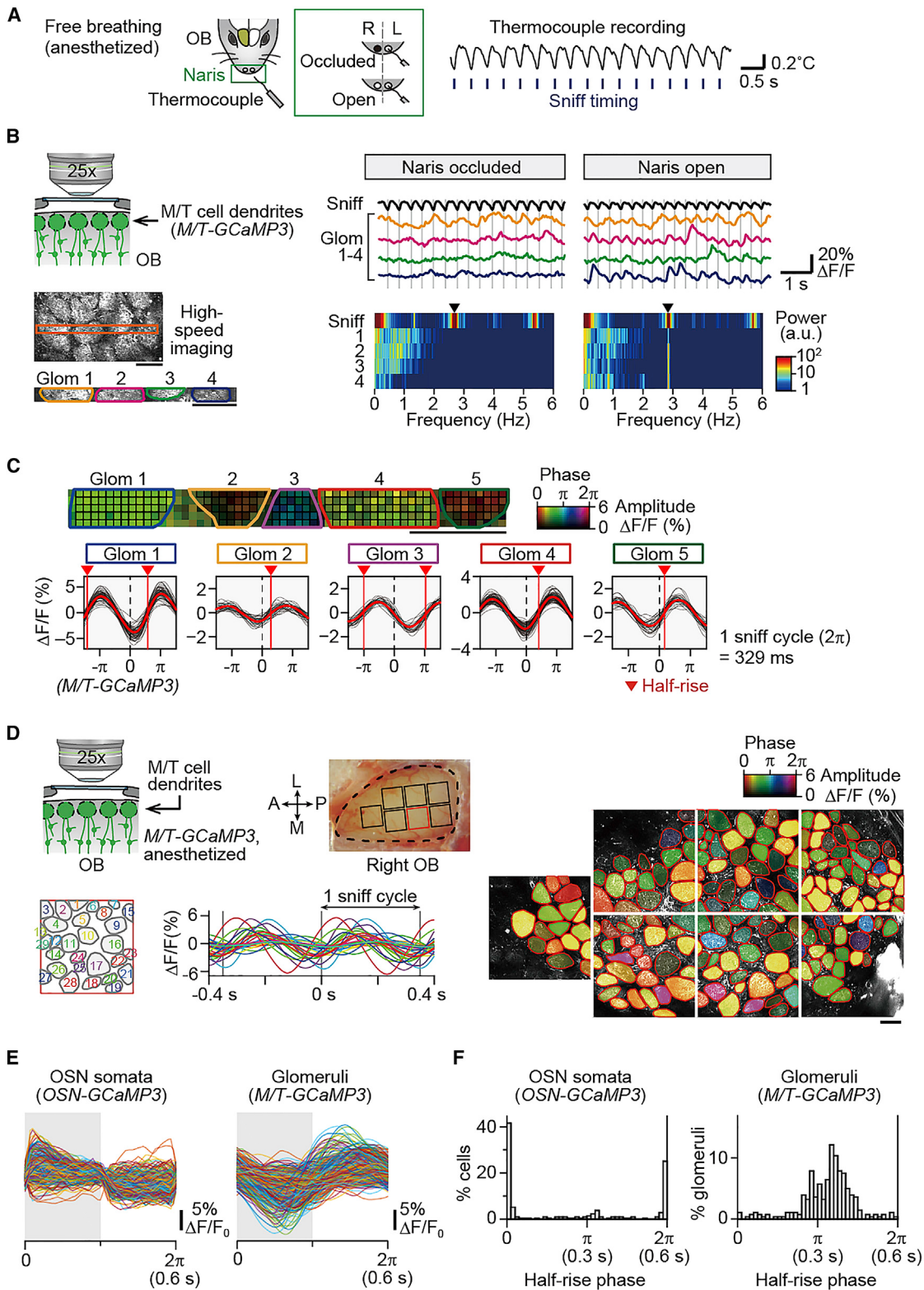


Figure 2. Glomerulus-Specific Oscillations Are Caused by Airflow-Induced Mechanosensation

(A) Recording sniff cycles. A thermocouple was located at the opening of the contralateral nostril to the imaging side. Nasal occlusion was performed for the nostril ipsilateral to the imaging side. The sniff timing was determined by the local minima of thermocouple measurements.

(legend continued on next page)

optical window in the nasal bone. In the OE, odorants typically produced sparse responses in OSNs; however, airflow stimuli produced robust and widespread responses (Figure 1C). In OSN axon terminals located in the OB, airflow-driven responses were variable and unique to each glomerulus (Figure 1D), suggesting that the extent of the mechanosensitivity is OR specific, as has been reported previously (Carey et al., 2009; Connelly et al., 2015; Grosmaire et al., 2007). The overall amplitude became higher as flow rate increased (Figure 1D). Typically, ~50% of glomeruli demonstrated significant increases in GCaMP3 fluorescence ($p < 0.01$, one-tailed t test), consistent with earlier patch-clamp recording of OSNs (Grosmaire et al., 2007). To observe mechanosensory responses of M/T cells, we also performed calcium imaging of *Pcdh21-Cre*; CAG-STOP-GCaMP3 (Ai38) (Wachowiak et al., 2013; Zariwala et al., 2012) and *Thy1-GCaMP6f* (GP5.11) (Dana et al., 2014) mice, in which GCaMP3 and GCaMP6f are specifically expressed in M/T cells, respectively (*M/T-GCaMP3* and *M/T-GCaMP6f* hereafter; Figure S1). It has been demonstrated that GCaMP signals at M/T cell dendrites represent action potentials at the somata (Wachowiak et al., 2013), although we cannot exclude possible contribution of synaptic NMDAR activity and dendritic spikes. Like OSN-GCaMP3 mice, *M/T-GCaMP3* displayed robust and widespread responses to the nasal airflow in the glomerular layer (Figure 1E). In M/T cells, ~80% of glomeruli demonstrated significant excitatory responses to the onset of nasal airflow ($p < 0.01$, one-tailed t test), which was higher than the percentage of OSNs that responded (Figures 1D and 1E). However, the excitatory responses were not as persistent as was observed in OSNs and gradually declined (Figure 1E), suggesting that the M/T cells are more sensitive to temporal changes in airflow conditions.

Glomerulus-Specific Oscillations by Mechanosensation

Mechanosensation in OSNs is necessary to produce the sniff-coupled oscillatory activity, also known as theta oscillations, in M/T cells. When nasal airflow was prevented by reversible unilateral naris occlusion, M/T cell dendrites in glomeruli demonstrated spontaneous and sporadic neuronal activity. However, under rhythmic nasal airflow, most glomeruli demonstrated oscillatory neuronal activity, which was coupled to the sniff cycles (Figures 2A and 2B), recorded by a temperature sensor located at the opening of the nostril (Kepcs et al., 2007). Power

spectrum analysis of the M/T cell activity yielded a peak at the sniff frequency in this condition (Figure 2B).

Next, we sought to determine the precise phases of the sniff-coupled oscillations. We determined the average response from traces registered to the sniff timing. The half-rise timing was determined from averaged fluorescence traces, since the fluorescence rise time (τ_{on}) is fast and constant across a wide range of firing rates, unlike the slower decay time (τ_{off}) (Chen et al., 2013; Wachowiak et al., 2013). Thus, the half-rise timing can be best used to estimate the timing of burst firing. The oscillations were synchronized within a glomerulus (Figure 2C), consistent with earlier findings of synchrony among “sister” M/T cells associated with a common glomerulus (Hayar et al., 2005; Schoppa, 2006; Schoppa and Westbrook, 2001). However, different glomeruli oscillated at different phases relative to the sniff cycle (Figure 2D; Movie S1). These different phases were arranged in an apparent mosaic pattern in the glomerular layer (Figure 2D). We also obtained similar results for M/T cell somata (Figure S2D).

Interestingly, such variable oscillation phases were not evident at the level of OSN somata. In the OSN somata, the GCaMP signals were high and low during airflow-on and -off periods, respectively, showing binary changes (Figures 2E and 2F). Thus, the glomerulus-specific variable oscillation phases are likely produced in the OB circuits.

Artificial sniffing at different frequencies (1–10 Hz) produced oscillations at the corresponding frequencies; as a result, the temporal response patterns of glomeruli were slightly “compressed” at higher frequencies (Figures 3A–3C). These glomerulus-specific oscillations were also observed in head-fixed awake animals running on a treadmill (Figure 3D). Due to the dynamic nature of the sniff conditions in awake animals, the basal fluorescence levels were highly fluctuating (Figures 3E–3G), consistent with recent studies (Blauvelt et al., 2013; Kato et al., 2013); however, the temporal response sequence of glomeruli was preserved across the physiological 1–10 Hz range (Figures 3H and 3I).

Phase Coding Distinguishes Odor from Mechanical Signals

Nasal airflow is essential for sampling odors, and indeed, the sniff speed is actively controlled to improve sensitivity to an

- (B) Calcium dynamics of M/T cell dendrites in naris-occluded and -open conditions in a freely breathing, anesthetized *M/T-GCaMP3* mouse. GCaMP3 traces (imaging frame rate, ~20 Hz) are shown along with sniff timing (gray vertical lines; see STAR Methods for details). Multi-taper spectra of the glomerular activity (bottom, data from a 2-min recording) showed peaks at the sniff frequency (~3 Hz, arrowhead), only in naris-open conditions.
- (C) Sniff-coupled oscillatory activity of five glomeruli in a freely breathing, anesthetized *M/T-GCaMP3* mouse. The oscillation phase of GCaMP3 signals was largely consistent within a glomerulus but heterogeneous among different glomeruli (a 4-min recording, 727 sniff cycles in an anesthetized mouse). The half-rise phases relative to the sniff timing are color-coded for individual image units (top, 4 × 4 pixel binned). Cycle-averaged oscillation traces for individual image units (bottom, gray traces) and glomeruli (red traces) are shown on the bottom. Red vertical lines with arrowheads indicate the half-rise phase.
- (D) Oscillation phases of glomeruli (M/T cell dendrites) in the dorsal OB of a freely breathing, anesthetized *M/T-GCaMP3* mouse. Oscillation traces for glomeruli in the middle are cycle-averaged from 6 s recordings (~17 sniff cycles; STAR Methods). The oscillation half-rises relative to sniff timing and the oscillation amplitudes are color-coded for 186 glomeruli in the bottom. See also Movie S1.
- (E) Cycle-averaged traces for the mechanosensory responses in the OSN somata in the OE and M/T cell dendrites in glomeruli. Pre-odor period for experiments shown in Figures S2E–S2H was used for OSN somata data ($n = 256$ cells in $n = 4$ OSN-GCaMP3 mice, trial-averaged). The dataset for glomeruli is from the pre-odor period for odor experiments shown in Figures 4C–4E (*M/T-GCaMP3* mice, single trial).
- (F) Histograms of the half-rise phases of the mechanosensory responses in OSN somata ($n = 212$ cells) and M/T cell dendrites ($n = 280$ glomeruli). Note that half-rise phases are close to the airflow onset timing in the OSN somata, but are later and more variable in the M/T cells.
- Scale bars, 100 μ m.

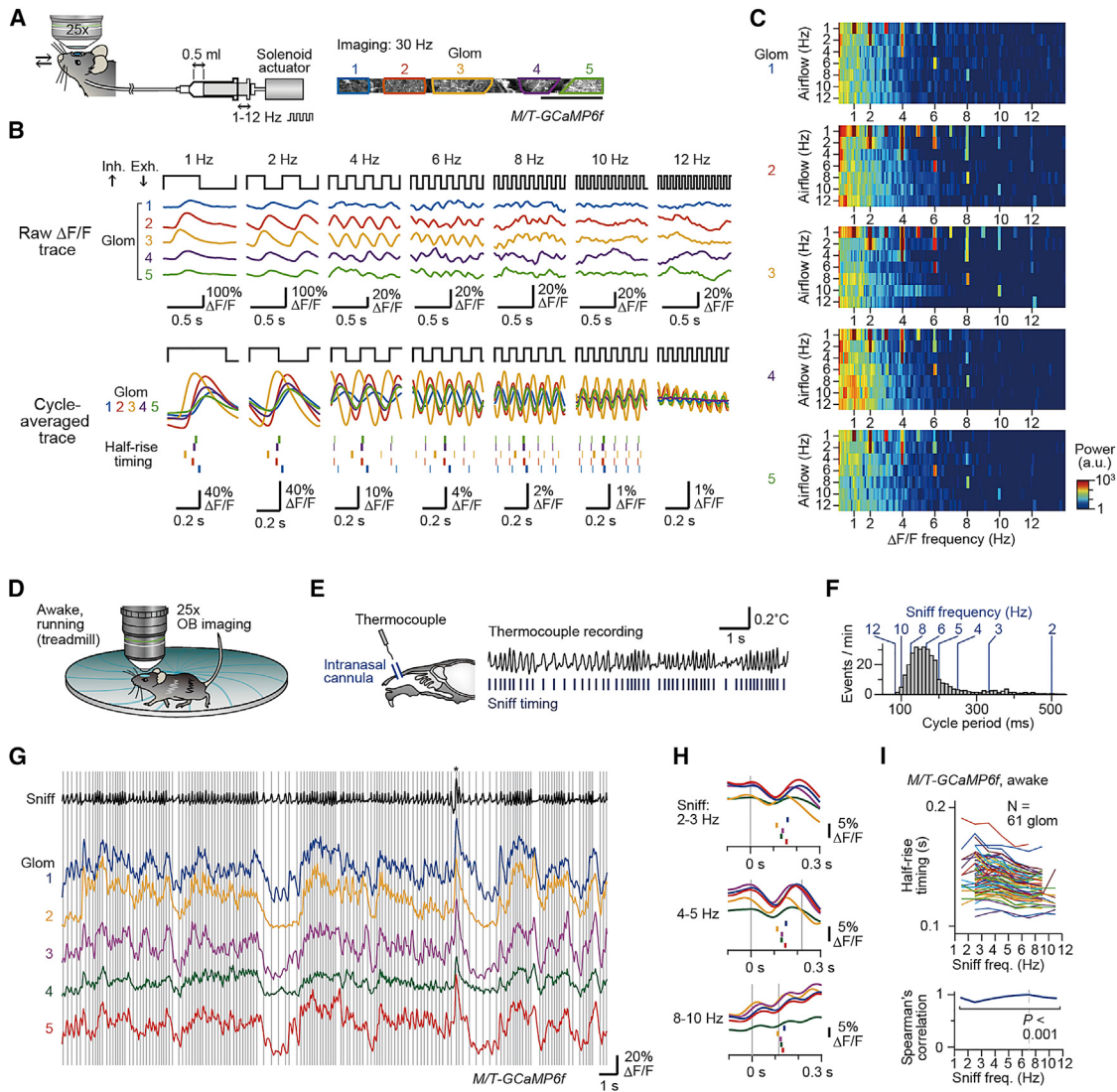


Figure 3. Sniff-Coupled Oscillations Are Consistent across Sniff Frequencies

(A) M/T cell dendrites were imaged in an *M/T-GCaMP6f* mouse during 1–12 Hz artificial sniffing. Airflow was generated by a syringe pump with a solenoid actuator. The working volume of the pump was adjusted to 0.5 mL/stroke. Scale bar, 100 μ m.

(B) Raw activity traces (top) and cycle-averaged traces (bottom). The temporal sequence of the half-rise timing (shown by vertical bars) was largely maintained up to 10 Hz.

(C) Multi-taper spectra of raw $\Delta F/F$ data for 1–12 Hz artificial sniffing conditions. The raw activity data for each of 1–12 Hz artificial sniffing were obtained from 20 s imaging sessions.

(D) Schematic of *in vivo* imaging performed in an awake *M/T-GCaMP6f* mouse running on a circular treadmill.

(E) Sniff cycles were recorded with an intranasal cannula in awake mice. Sniff timing was defined by the local maxima of thermocouple measurements.

(F) Histogram of sniff frequency in an 8-min imaging session. The peak frequency range (6–8 Hz) was used as a reference for correlation analysis in (I).

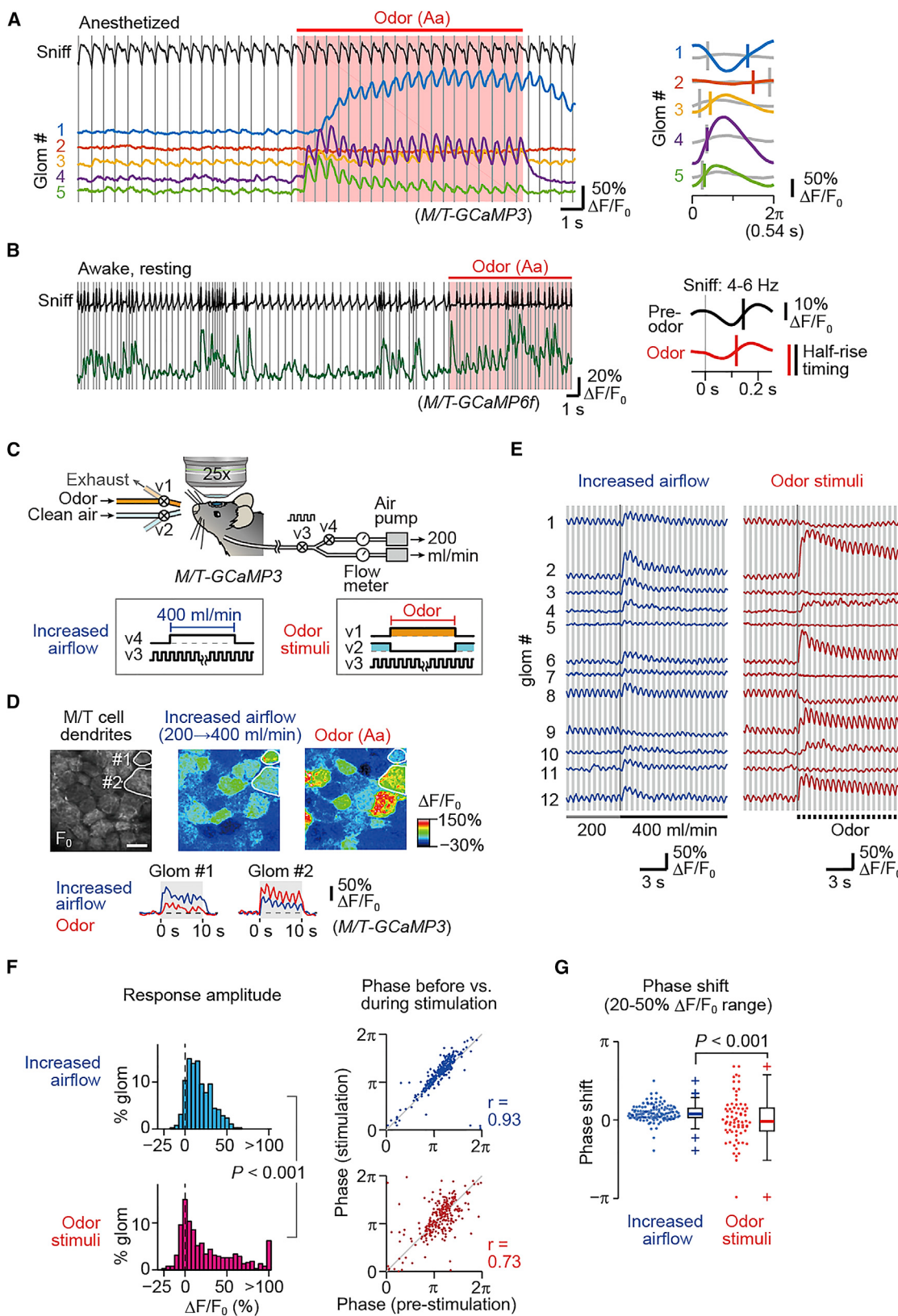
(G) Raw fluorescence traces in M/T cell dendrites in an awake *M/T-GCaMP6f* mouse running on a circular treadmill. Sniff timing is indicated by gray vertical lines. Note that large airflow responses were induced by sighing (asterisk).

(H) Cycle-averaged oscillation traces and the half-rise timing in different sniff frequency ranges (from the 8-min recording). The temporal pattern of oscillation phase was maintained up to 8–10 Hz sniffing. Mean sniff timing is indicated by gray vertical lines (STAR Methods).

(I) Top: oscillation half-rise timing relative to sniff timing for 61 glomeruli. Bottom: the temporal sequences of oscillation half-rise timing were evaluated by Spearman's correlation coefficients to the most typical 6–8 Hz range.

odor in behaving animals (Kepcs et al., 2007; Oka et al., 2009; Verhagen et al., 2007). However, our results show that changes in sniff conditions inherently produce large background signals in many glomeruli (Figure 3G). In such situations, many glomeruli

would have difficulty in distinguishing between odor signals and mechanical signals. How can odor-evoked signals be distinguished from the airflow-produced mechanosensory responses? It has been known that odors activate M/T cells at



(legend on next page)

specific timings within a sniff cycle (Bathellier et al., 2008; Cury and Uchida, 2010; Macrides and Chorover, 1972; Spors and Grinvald, 2002), and behaving mice can also discriminate the temporal differences produced (Smear et al., 2013). Indeed, we observed odor- and glomerulus-specific phase shifts in sniff-coupled oscillations (phase coding) (Kepecs et al., 2006; Panzeri et al., 2010), with both advances and delays, in anesthetized (Figures 4A and S3A–S3C) and awake (Figures 4B and S3D) animals. We also observed odor-evoked phase shifts in M/T cell somata (Figures S3F and S3G). Furthermore, correlations between odor-evoked response amplitudes (mean $\Delta F/F_0$ of GCaMP signals; rate code) (Chen et al., 2013; Wachowiak et al., 2013) and phase shifts (shifts in half-rise timing within a sniff cycle; phase code) were typically very weak (Figure S3H), raising the possibility that phase coding behaves differently from rate coding. In fact, this result was in contrast to earlier predictions, in which response latency should be inversely correlated with the firing rate (Brody and Hopfield, 2003; Hopfield, 1995; Margrie and Schaefer, 2003). We therefore considered the possibility that mechanical and odor stimuli have distinct impacts on the phase coding.

Here we compared the changes in phase code (half-rise timing) between mechanical and odor stimuli using artificial sniffing. To increase mechanical stimuli, we changed the airflow speed from 200 to 400 mL/min (Figure 4C). Increases in airflow speed induced widespread increases in GCaMP3 fluorescence (rate code) across many glomeruli (Figures 4D and 4E; Movie S2), in contrast to the sparser responses produced by the odor stimuli (Figure 4F, left; $p < 0.001$, Kolmogorov-Smirnov test). However, increases in airflow speed were only accompanied by small changes in the phase code (Figure 4F, right). When we analyzed glomeruli with 20%–50% $\Delta F/F_0$ changes, odor produced significantly larger changes in phase (Figure 4G; $p < 0.001$, Levene's tests for equal variance; see also Figure S3H). Thus, the phase coding in M/T cells only extracts odor signals, whereas the rate coding responds to both mechanical and odor stimuli.

Phase Coding Is Stable across Multiple Sniff Cycles

To further investigate the role of phase coding, we examined its stability in olfaction. The rate code patterns in M/T cells are

known to be dynamically reorganized and decorrelated within seconds (Bathellier et al., 2008; Kato et al., 2012; Niessing and Friedrich, 2010) (see also Figures 4A and 5A). For example, the rate code patterns at the first and last sniff cycles are very different in Figure 5B. We therefore compared the stability of rate code versus phase code across multiple sniff cycles. Since the first sniff is known to contain sufficient information for odor recognition in rodents (Uchida and Mainen, 2003), we examined how the rate and phase codes from the first sniff are preserved in subsequent sniff cycles. We determined the correlation at each sniff cycle relative to the first sniff for both the rate code (mean $\Delta F/F_0$) and phase code (shifts in half-rise phase/timing).

We analyzed the stability of rate code for 27 odors with various chemical structures (Figure S4A). The rate coding among glomerular populations gradually evolved over time, although its extent was variable among different odorants (Figure S4B). We then selected eight odors with different rate code stability and chemical structures for further analyses. We determined both the rate code and phase code for glomeruli showing odor-evoked amplitude changes and detectable oscillatory activities throughout sniff cycles (criteria were as follows: peak $\Delta F/F_0 > 40\%$, average oscillation amplitude in each cycle $> 5\%$). The Spearman's correlation coefficient of the rate code to that of the first sniff gradually decreased across multiple sniff cycles during the odor exposure period for 12 s, whereas the correlation of the phase code was maintained at higher levels (Figures 5A–5D and S5). While a single sniff has been known to be sufficient for odor discrimination after training (Cury and Uchida, 2010; Uchida and Mainen, 2003), repeated sniffing is essential for other types of behavior, such as olfactory learning and scent tracking. Our results show that the phase code is conserved across multiple sniff cycles and is more stable than the rate code (Figure 5E).

Phase Coding Is Concentration Invariant

For behaving animals in their natural environment, fluctuating odor concentrations are another big challenge for stable odor identification. The neural mechanisms that preserve concentration-invariant odor coding remain a long-standing issue in the field. Here we examined the stability of the phase code across

Figure 4. Odor Stimuli, but Not Airflow Changes, Produce Phase Shifts in Sniff-Coupled Oscillations

- (A) Odor-evoked responses of M/T cell dendrites (five glomeruli) in an anesthetized, freely breathing M/T-GCaMP3 mouse (Aa, amylacetate diluted at 1:2,000). Cycle-averaged traces and half-rise phases during pre-odor (gray) and odor periods (colored) are shown on the right.
- (B) M/T cell dendrite responses to an odor (Aa, amylacetate diluted at 1:200) in an awake M/T-GCaMP6f mouse resting in a body tube. Cycle-averaged traces and the half-rise timing in pre-odor and odor periods are shown on the right (4–6 Hz sniff frequency range). See also Figures S3A–S3E for additional examples in anesthetized and awake conditions. M/T cell somata showed similar results (Figures S3F and S3G).
- (C) Experimental setup for comparing airflow changes versus odor stimuli in tracheotomized M/T-GCaMP3 mice. For airflow changes (increases of the nasal airflow speed from 200 to 400 mL/min, 1.67 Hz), the nasal airflow speed was increased by opening valve 4 (v4). For odor stimulations (benzaldehyde and amylacetate diluted at 1:1,000; under artificial sniffing at 200 mL/min, 1.67 Hz), clean air (v2) was switched to odorized air (v3).
- (D) Representative responses to airflow changes and an odor (Aa, amylacetate). These stimuli were applied for 10 s (shown in gray). Scale bar, 100 μm . See also Movie S2.
- (E) Sniff-aligned single-trial responses of 12 randomly chosen glomeruli. The airflow-on periods are indicated by vertical stripes in gray.
- (F) Left: histograms of response amplitude for the first 3 s of stimulation. Combined data for benzaldehyde and amylacetate ($n = 387$ glomerulus-stimulus pairs from 11 mice; $p < 0.001$, Kolmogorov-Smirnov test). Right: changes of oscillation phase in 291 (airflow changes) and 264 (odors) glomerulus-stimulus pairs that were oscillatory both before and after stimulus onset. Pearson's correlation coefficient, “ r ,” is significantly different between the two responses; $p < 0.001$, two-tailed t test after Fisher's z transformation.
- (G) Boxplots of phase shifts for glomeruli showing 20%–50% $\Delta F/F_0$ ($n = 132$ and 72). Whiskers extend to the most extreme values within 1.5 times the interquartile range. Odor-induced phase shifts were more broadly distributed ($p < 0.001$, Levene's test for equality of variances). See also Figure S3H for scatterplots of mean response amplitude and phase shifts.

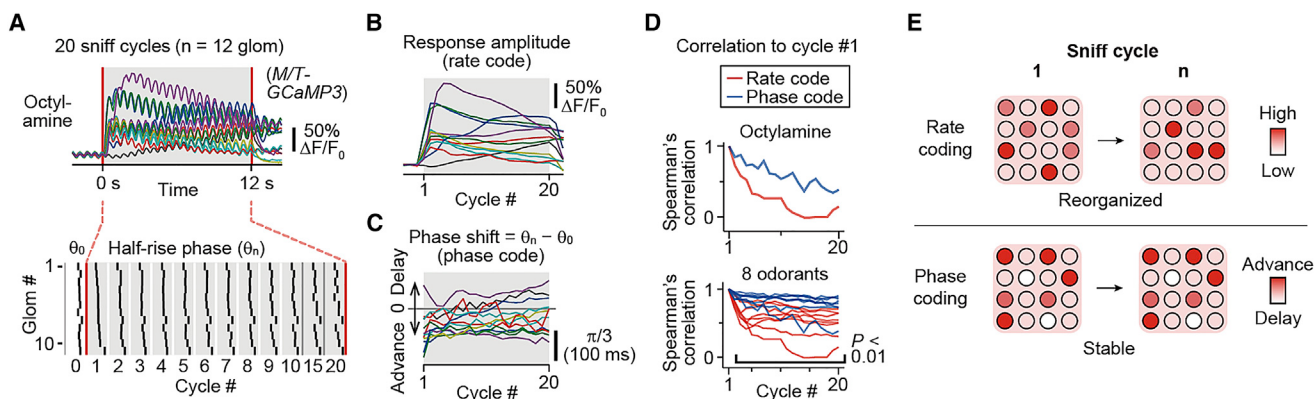


Figure 5. Phase Coding Is Consistent across Multiple Sniff Cycles

- (A) Responses to octylamine diluted at 1:100 over 12 s odor exposure periods (20 sniff cycles; gray) in tracheotomized M/T-GCaMP3 mice. Artificial sniffing was performed at 200 mL/min and 1.67 Hz. Top: mean traces from five trials ($n = 12$ glomeruli from 3 mice). Bottom: half-rise phase in each cycle is indicated by vertical bars before (θ_0) and during odor stimulations (θ_n , $n = 1-20$). See also Figure S5 for the seven other odors.
- (B) Mean $\Delta F/F_0$ in each cycle (rate code) during stimulation with octylamine. See also Figures S4 and S5 for all 27 odors.
- (C) Oscillation phase shifts ($\theta_n - \theta_0$; phase code) during responses to octylamine. See also Figure S5 for seven other odors.
- (D) The temporal dynamics of phase code (blue) and rate code (red) were analyzed using Spearman's correlation coefficients to the reference cycle (cycle #1) for octylamine (top) and total of eight odorants (bottom). The stability of phase code was higher than that of rate code ($p < 0.01$ from third to last odor cycle, Wilcoxon signed-rank test).
- (E) A schematic summary for temporal reorganization of rate code versus stable phase code.

odor concentrations. We recorded M/T cell responses for 14 different odors (10 pure odorants and 4 mixed odors) at 5 different concentrations (1:100–1:8,100 dilutions). Although many glomeruli showed tonic concentration-dependent increases in the rate code, this was not always the case. For other glomeruli, glomerular response patterns in the rate code were concentration specific, and some glomeruli that responded at a lower concentration were not always responsive at higher concentrations (Figures 6B and S6A). Thus, the rate code pattern tends to be reorganized as the odor concentration changes. As for the phase coding, increasing odor concentrations caused both phase advance and delay (Figures 6B and S6B). Unlike rate coding, however, the phase advance or delay was consistent at a wide range of odor concentrations. As a result, odor-evoked phase shifts were concentration invariant. We evaluated concentration-dependent pattern changes using Spearman's correlation coefficient to the responses at the highest concentration (1:100 dilution) for all odors. As for the rate code, the correlation decreased as the concentration differences increased (Figures 6C and S6C; the median correlation between lowest versus highest concentrations was 0.23, $n = 14$ odors). Unlike rate coding, however, phase coding was consistent at a wide range of odor concentrations, and this correlation was maintained at higher levels (median correlation, 0.82 versus 0.23) (Figures 6C and S6C). Thus, phase coding is more consistent across concentrations than rate coding.

We also used classifier models based on the Euclidian distance in the rate/phase coding spaces to examine which coding strategy is more effective in discriminating (or “decoding”) odors in a concentration-invariant manner (Miura et al., 2012). In these coding spaces, each glomerulus contributes to a dimension, and the value in that dimension was either the rate code or the phase code. Classification success rate (decoding performance) was

higher with phase coding than with rate coding (Figures 6D and S6D). Similar results were obtained with a linear classifier based on support-vector machine (Figure S6E). Together, these findings show that phase coding is a powerful strategy for concentration-invariant odor identification (Figures 6E and 6F).

Mechanosensation Facilitates Robust Phase Coding of Odors

While phase coding can distinguish between odor and mechanical signals, could mechanosensation in OSNs be beneficial for olfaction? Since odor is delivered by rhythmic nasal airflow, one might argue that a rhythmic application of an odor could be sufficient to produce the temporal patterns without mechanosensation. To directly test the role of mechanosensation, we compared the single-trial odor-evoked responses of M/T cells in the presence and absence of oscillatory mechanosensation (six trials each). Using an artificial sniffing preparation, we evaluated odor-evoked responses under two conditions: (1) where both mechanical and odor stimuli were rhythmically applied to the OE ($m+$) to recapitulate physiological odor sampling conditions and (2) where pulsed odor stimuli were applied under continuous airflow ($m-$) to specifically eliminate mechanosensory oscillations (Figure 7A). Some of the glomeruli were activated with the same timing between these conditions, indicating that odor was delivered to the OE in a similar timing (Figure 7B; see also Figure S7A, indicating quick odor switching in this setup); however, many other glomeruli demonstrated delayed responses under $m-$ conditions (Figures 7B, S7B, and S7C). More importantly, we found that the phase code was more precise (i.e., less variable across trials) under $m+$ conditions than in $m-$ conditions (Figures 7A, 7B, and S7B–S7D). As a result, the decodability of odor identity with the distance-based classifier (Figure 6D) was higher under $m+$ conditions than in

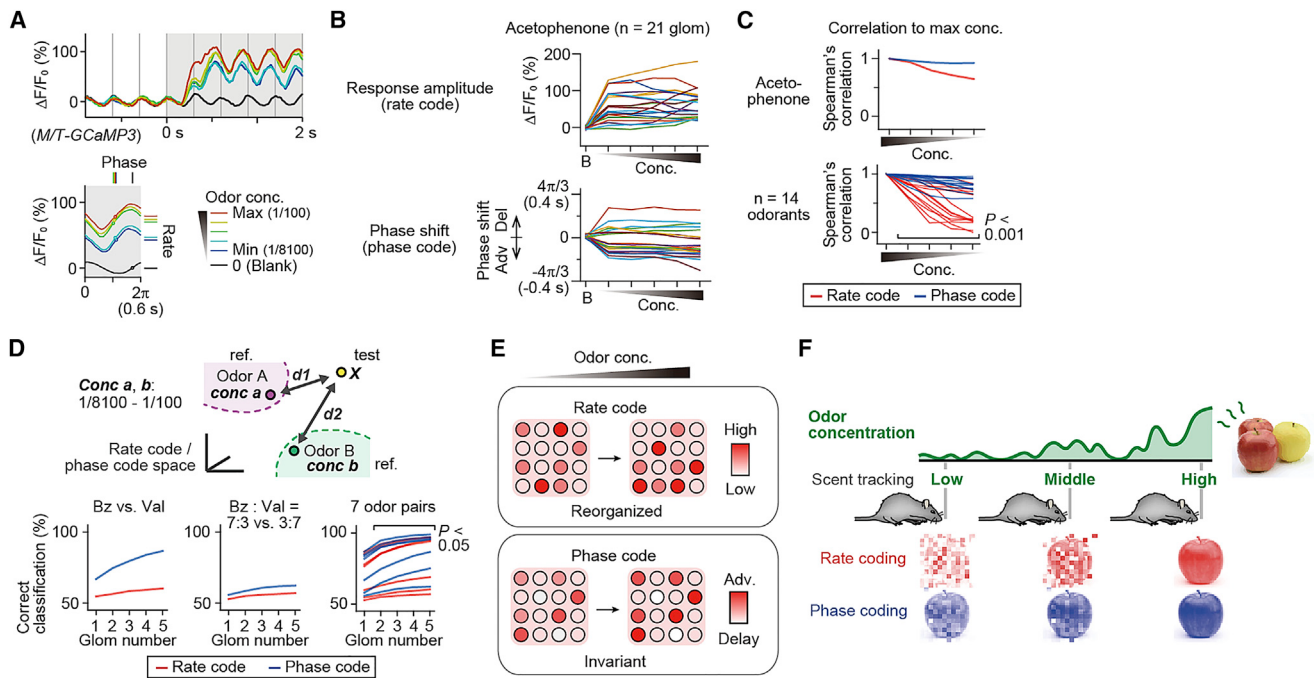


Figure 6. Concentration-Invariant Phase Coding

(A) Representative responses of a glomerulus to serially diluted odors (1:8,100, 1:2,700, 1:900, 1:300, and 1:100; valeraldehyde) in a tracheotomized *M/T-GCaMP3* mouse. Artificial sniffing was performed at 200 mL/min and 1.6 Hz. The gray shaded area indicates the odor stimulation period. Sniff onset is indicated by gray vertical lines.

(B) Concentration response curves for acetophenone ($n = 4$ mice). Response amplitude (left) and oscillation phase shifts (right) for blank (B) and odor trials (1:8,100–1:100, data are from initial 6 s). See also Figures S6A and S6B for 13 other odors.

(C) Concentration-dependent dynamics of ensemble rate code (red) and phase code (blue) were evaluated by Spearman's correlation coefficients. The highest concentration (1:100) was used as a reference. Stability across concentrations was higher for phase code than rate code ($p < 0.001$ from 1:8,100 to 1:300, Wilcoxon signed-rank test).

(D) Classification of two odors by rate code (mean $\Delta F/F_0$ during the first 6 s) or phase code (mean phase for the first 6 s, relative to the sniff timing) using a Euclidean distance-based classifier (see STAR Methods for details). Top: schematic of classification analysis to compare decoding performance of rate code versus phase code. A rate or phase code in each glomerulus contributes to a dimension. For each trial, one out of five concentrations was randomly chosen for each of the odors to serve as a reference. A test odor was randomly chosen from the remaining data. Bottom: results are means of 50,000 random trials. The phase code showed a similar or higher performance in concentration-independent classification of odor identities ($p < 0.05$ for classification using 2–5 glomeruli, Wilcoxon signed-rank test). Chance levels are 0.5. Bz, benzaldehyde; Val, valeraldehyde.

(E) Schematic diagram showing reorganization of rate code patterns and concentration-invariant phase coding.

(F) A proposed role of phase coding in olfaction. Concentration-invariant phase coding may be useful for odor identification under fluctuating sampling conditions and aid scent-tracking behavior, for example. In contrast, rate code patterns are not preserved at different odor concentrations.

$m-$ conditions (Figures 7D and S7E). In addition, the response amplitude was larger under $m+$ (Figures 7A and 7B). Notably, mechanosensation was particularly important for robust phase coding when odor concentrations were lower, which are challenging conditions for odor identification (Figures 7C, S7C, and S7D).

We also examined the stability of phase codes under $m+$ and $m-$ conditions. The phase code correlation to the first sniff was maintained at higher levels throughout multiple sniff cycles under $m+$; however, the correlation tended to decrease from second sniff cycle under $m-$ conditions (Figures 8 and S8). Thus, sniff-coupled mechanosensation in OSNs is important for robust phase coding of odor identity (Figure 8D).

DISCUSSION

While the temporal representation of odor signals in M/T cells has been known for many years (Cury and Uchida, 2010; Macr-

ides and Chorover, 1972; Shusterman et al., 2011; Spors and Grinvald, 2002; Wellis et al., 1989), and various hypotheses have been proposed (Friedrich, 2013; Hopfield, 1995; Kepcs et al., 2006; Laurent, 2002; Uchida et al., 2014; Wilson and Mainen, 2006), the roles of temporal patterning have remained unclear. For example, some proposed that odor identity is encoded in the temporal patterns (Cury and Uchida, 2010; Spors and Grinvald, 2002), while others proposed that these patterns encode odor intensity (Margrie and Schaefer, 2003; Sirotin et al., 2015). In the present study, we performed a comprehensive analysis under more physiological conditions and demonstrated that the phase coding of M/T cells is stable across various sniff conditions (frequency and speed), multiple sniff cycles, and a wide range of odorant concentrations. We thus propose that the phase coding is the basis for the invariant encoding of an odor identity under fluctuating sampling conditions, which is useful for the scent tracking behavior, for example (Figure 6F).

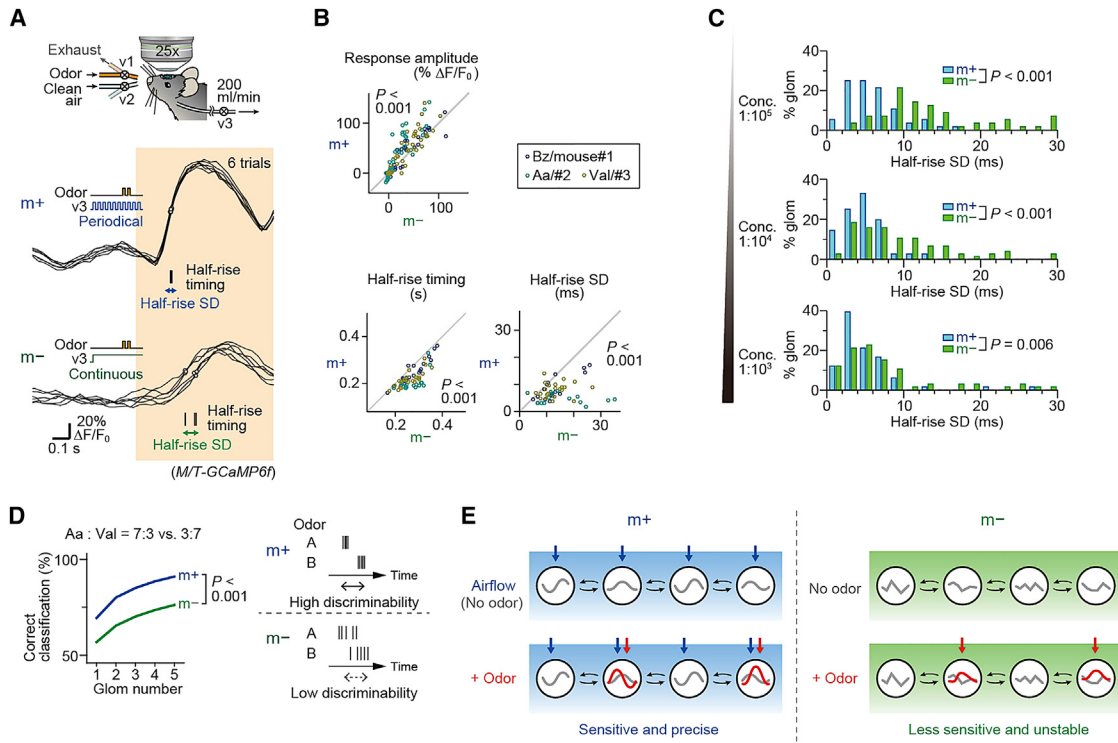


Figure 7. Mechanosensory Oscillations Are Required for Robust Phase Coding of Odors in M/T Cells

(A) Mechanosensory oscillations were either produced by periodical air suction (m+; pulsed airflow at 200 mL/min and 1.67 Hz) or eliminated by continuous suction (m-; airflow at 200 mL/min) in tracheotomized *M/T-GCaMP6f* mice. In the m- condition, odorized (v1) and clean (v2) air was delivered alternately for pulsed odor exposure. Three-way solenoid valves (v1 and v2) were used to keep the air pressure constant. Note that odor was delivered to the OE with approximately the same timing between these two conditions (Figures S7A and S7C). Representative responses of a glomerulus to an odor (amyacetate diluted at 1:100,000; odor application is indicated by the shaded area) are shown for six trials in m+ and m- conditions. Half-rise SD is defined as the variability (standard deviation) of half-rise timing across six trials. See also Figure S7B for other representative examples.

(B) m+ conditions showed larger response amplitudes ($p < 0.001$, Wilcoxon signed-rank test; $n = 114$ glomeruli), faster half-rise timing ($p < 0.001$, Wilcoxon signed-rank test; $n = 61$ glomeruli), and a smaller variability of half-rise timing ($p < 0.001$, Wilcoxon signed-rank test; $n = 56$ glomeruli). Different colors represent three odorants diluted at 1:100,000 (Bz, benzaldehyde; Aa, amyacetate; Val, valeraldehyde). Data for each odorant were obtained from single animals ($n = 3$ mice). See also Figure S7C for two other odor concentrations. Note that half-rise timing is almost identical between m+ and m- for subsets of glomeruli (middle panel, data points along the unity line), indicating that timing of odor delivery to the OE is the same between m+ and m-. See also Figure S7A.

(C) Histogram of half-rise SDs in three different odor concentrations. Data for individual mouse-odor samples are shown in Figures S7C and S7D.

(D) Classification of two odors by single-trial phase code (response half-rise timing) using a Euclidean distance-based classifier. Each glomerulus contributes to a dimension. For each classification trial, one out of six trials was chosen for each of the odors to serve as a reference. A test odor was chosen from the remaining odor trials. Results are the means of classification trials with all the possible combinations of 1–5 glomeruli from $n = 22$ glomeruli dataset (22–26,334 combinations). The classification success rate was significantly higher in m+ conditions ($p < 0.001$, χ^2 test). Chance levels are 0.5. Aa, amyacetate; Val, valeraldehyde. Total concentrations of odorant mixtures were 1:100,000. See also Figure S7E. Right: schematic summary of the precise phase coding and higher discriminability under m+ conditions.

(E) A possible network model of robust phase coding by airflow-driven mechanosensory oscillations. Mechanosensory oscillations (gray lines) in glomeruli (black circles) aid sensitive and temporally precise responses to odors (m+), possibly due to inhibition and disinhibition among glomeruli. In the absence of mechanosensory oscillations, however, the baseline neuronal activity is fluctuating, and as a result, the odor-evoked responses become unstable (m-).

In contrast, rate coding is an excellent candidate for odor intensity coding.

Previously, temporal patterns in M/T cells have been considered to be due to differential response latencies to odor stimuli. In this study, however, we demonstrated that the glomerulus-specific mechanosensory oscillations are the underlying basis for the temporal patterns (Figures 7 and 8), and that the temporal patterns are only evident in M/T cells (Figures 2E, 2F, and S2). In addition, some examples showed phase shifts without rate code changes (Figure 4A). Thus, the temporal patterns would be best understood as phase shifts (phase coding) in the mechanosen-

sory-based oscillations (Figure 8D). Notably, however, we do not intend to argue that the relative timing in a cycle, rather than the absolute time from the stimulus onset, is the code utilized in this system. In fact, this issue has been debated in previous studies. For example, it has been reported that M/T cells show similar response latencies between slow and fast sniffs (Carey and Wachowiak, 2011; Cury and Uchida, 2010). However, another study reported that the relative timing (phase) in a sniff cycle is more consistent than the absolute timing (Shusterman et al., 2011). Due to the relatively slow kinetics of GCaMPs, it is difficult to conclude which is the case in the present study.

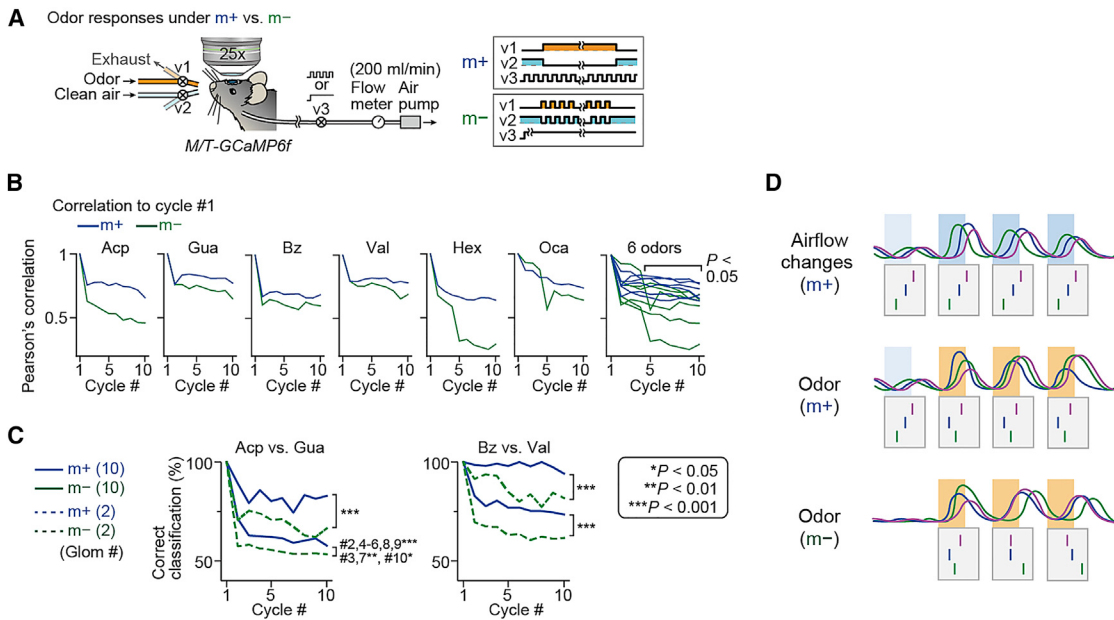


Figure 8. Stability of Phase Coding across Multiple Sniff Cycles with and without Mechanosensory Oscillations

(A) Experimental configurations for *m+* and *m-* conditions, performed in tracheotomized *M/T-GCaMP6f* mice. Sniff-coupled mechanosensory oscillations were produced by periodical suction in the *m+* condition (pulsed airflow at 200 mL/min and 1.67 Hz) but eliminated in the *m-* condition (continuous airflow at 200 mL/min).

(B) The stability of the ensemble phase code for six odors. Half-rise phase in each sniff cycle was determined for acetophenone (AcP; diluted at 1:100; $n = 63$ glomeruli from $n = 3$ mice in both *m+* and *m-*), guaiacol (Gua; diluted at 1:1,000; $n = 68$ and 66 pairs from $n = 3$ mice in *m+* and *m-*, respectively), benzaldehyde (Bz; diluted at 1:100; $n = 60$ and 55 pairs from $n = 5$ mice), valeraldehyde (Val; diluted at 1:100; $n = 62$ and 57 pairs from $n = 5$ mice), hexanoic acid (Hex; diluted at 1:100; $n = 36$ and 35 pairs from $n = 2$ mice), and octylamine (Oca; diluted at 1:100; $n = 36$ and 29 pairs from $n = 2$ mice) (see Figure S8). Then, Pearson's correlation coefficients to cycle #1 were determined for each sniff cycle. Note that the correlation was higher in *m+* condition than in *m-* condition ($p < 0.05$, Wilcoxon signed-rank test).

(C) Classification of two odors (AcP versus Gua and Bz versus Val) by phase code using a Euclidean distance-based classifier. The first odor cycle was used as a reference, and a test odor was chosen from the remaining cycles. Results are the mean of each cycle using random combinations of two or ten glomeruli. Classification success rate was significantly higher in *m+* conditions ($p < 0.001$, χ^2 test).

(D) Schematic summary of the results. Sniff-coupled mechanosensation in OSNs produces glomerulus-specific oscillatory activity in M/T cells. The glomerulus-specific oscillatory phases are unaffected by changes in airflow speed; however, odor stimuli causes the phase shifts, which are stable across multiple sniff cycles. The stability of the phase coding is impaired without rhythmic mechanosensory inputs from OSNs (*m-*). The mechanosensory-based oscillations are also important for the precise phase coding across trials (Figure 7).

However, the results seem to be between the two scenarios. When sniff frequencies were increased, the temporal patterns of mechanosensation were compressed. However, at low-frequency ranges, the responses do not seem to fully tile the sniff cycles (Figures 3B, 3H, and 3I). This may be in good agreement with a recent study showing that the olfactory cortex reads out the “relative time code” in the OB with some temporal flexibility (Haddad et al., 2013).

Independent phase and rate coding have been known to occur in hippocampal place cells. The activity of place cells is locked to the hippocampal theta oscillations. While rate code in place cells reflects the action of animals, e.g., running speed, their theta phase patterns code the relative position of the target place and advance as the animal goes across the target, known as phase precession (Huxter et al., 2003). The phase information in hippocampal theta oscillations enables temporal cell assembly sequences, which form the basis for the spatial navigation and memory formation (Buzsáki and Moser, 2013). In contrast, in M/T cells, the sniff-coupled oscillation phase is unique to the

odor and invariant during repeated odor sampling. We also showed that phase coding can discriminate between odor and sniff-induced mechanical signals. This strategy is analogous to the whisker system, in which touch and self-motion are discriminated by phase coding (Kleinfeld and Deschênes, 2011; Severson et al., 2017). Thus, phase coding may be a general strategy for discriminating between sensory signals and active sampling itself. Recent studies suggested that the relative timing of M/T cells can be decoded in the piriform cortex, where neurons function as temporal coincidence or sequence detectors for different glomeruli (Franks and Isaacson, 2006; Haddad et al., 2013). Thus, the different temporal patterns in the OB are converted to the different ensembles of neurons in the piriform cortex, which are enforced by recurrent networks and in turn control robust behavioral outputs (Choi et al., 2011). Odor intensity might be simply represented by the firing rate of the same ensembles in the piriform cortex. In this scenario, a major function of the OB is to transform noisy sensory signals to a more reliable phase code for subsequent decoding of odor identity in the piriform cortex

(Kepes et al., 2006; Wilson and Mainen, 2006). However, we do not argue that phase coding is the sole mechanism for the odor identity coding. Rather, it is possible that rate coding is a basic strategy, and that phase coding is an additional mechanism used to ensure the coding reliability under fluctuating odor sampling conditions, including concentration invariance. It is also possible that the identity of some special odorants, such as innately attractive/aversive odorants and pheromones/kairomones, is encoded by the rate coding in specialized sets of glomeruli; accordingly, different areas of the olfactory cortex may use different decoding strategies.

Our study also demonstrated that mechanical stimulus, another sensory modality detected in OSNs, is utilized for odor coding in M/T cells (Figure 7E). This result was unexpected from earlier models for “latency” coding in M/T cells (Brody and Hopfield, 2003; Hopfield, 1995; Margrie and Schaefer, 2003). These models assumed that increasing sensory inputs leads to a shorter response latency based on the intrinsic oscillations of M/T cells; in such a case, mechanosensory inputs should behave similarly to odor and thus would simply obscure odor coding in M/T cells. However, we found that increase in mechanosensation does not change the phase, and rather facilitates the robust odor coding. In addition, we showed that phase coding (both phase advance and delay) behaves almost independently from the rate coding and that phase coding is more invariant across odor concentrations than the rate coding, directly contradicting earlier models. Thus, the OB circuit has a mechanism to maintain the phase code irrespective of the stimulus intensity, even at marginal concentration ranges. Proposed underlying mechanisms include intrinsic firing properties of M/T cells, subthreshold oscillations, and/or interglomerular inhibitory circuitry (Fukunaga et al., 2014; Hayar et al., 2005; Hopfield, 1995; Margrie and Schaefer, 2003; Schaefer et al., 2006). While the temporal patterns have been often described in OSN axons (Carey et al., 2009; Spors et al., 2006; Verhagen et al., 2007), Ca^{2+} dynamics at OSN axons are in fact heavily modulated by presynaptic inhibition and do not faithfully represent presynaptic component. In the present study, we examined the temporal patterns in OSN somata in the OE and found that temporal patterns were less evident in OSN somata (Figures 2E, 2F, and S2). This result indicates that the OB circuit may play a more important role in oscillations and phase coding. Identifying the exact network mechanisms of phase coding is an important issue for future studies.

STAR★METHODS

Detailed methods are provided in the online version of this paper and include the following:

- KEY RESOURCES TABLE
- CONTACT FOR REAGENT AND RESOURCE SHARING
- EXPERIMENTAL MODEL AND SUBJECT DETAILS
 - Mice
- METHOD DETAILS
 - Immunohistochemistry
 - Two-photon imaging
 - Measurement of sniff cycles

- Tracheotomy and artificial sniffing
- *In vivo* Ca^{2+} imaging
- Odor stimulations

● QUANTIFICATION AND STATISTICAL ANALYSIS

- Image analysis
- Oscillation analysis
- Power spectral analysis of sniff-coupled activity
- Responses to airflow changes versus odor stimuli
- Temporal dynamics of the population odor responses
- Rate- and phase- representations of odor concentrations
- Classification analysis
- Odor responses in the presence and absence of mechanosensory oscillations
- Statistical tests

● DATA AND SOFTWARE AVAILABILITY

SUPPLEMENTAL INFORMATION

Supplemental Information includes eight figures and two movies and can be found with this article online at <https://doi.org/10.1016/j.neuron.2017.11.008>.

AUTHOR CONTRIBUTIONS

R.I. performed all the imaging experiments and analyzed the data. H.K. performed microinjection for transgenesis. T.I. supervised the project. R.I. and T.I. wrote the manuscript.

ACKNOWLEDGMENTS

We thank Momo Fujii, Naho Atsumi, and Miwako Nomura for technical assistance; Kazushige Touhara for instruction on artificial sniffing; Takashi R. Sato and Tatsuo K. Sato for instruction on imaging in awake mice; Mineto Yokoi, Hongkui Zeng, and Karel Svoboda for mouse strains; and Marcus N. Leiwe, Takashi R. Sato, Keiji Miura, and Charles Yokoyama for critical reading of the manuscript. This work was supported by grants from the PRESTO program of the Japan Science and Technology Corporation (JST) (T.I.), the Sumitomo Foundation (T.I.), the Nakajima Foundation (T.I.), the Brain Science Foundation (T.I.), and the Japan Society for the Promotion of Science (JSPS) (KAKENHI 23680038, 15H05572, 15K14336, 16K14568, 16H06456, and 17H06261 to T.I.; 15K18353 to R.I.), and an intramural grant from RIKEN Center for Developmental Biology (T.I.). R.I. was supported by the Special Postdoctoral Researchers program of RIKEN and the JSPS postdoctoral fellowship. The imaging experiments were supported by the RIKEN Kobe Light Microscopy Facility. Animal experiments were supported by the Animal Resource Development Unit at the RIKEN Center for Life Science Technologies.

Received: July 12, 2017

Revised: October 13, 2017

Accepted: November 6, 2017

Published: December 6, 2017

REFERENCES

- Bathellier, B., Buhl, D.L., Accolla, R., and Carleton, A. (2008). Dynamic ensemble odor coding in the mammalian olfactory bulb: sensory information at different timescales. *Neuron* 57, 586–598.
- Blauvelt, D.G., Sato, T.F., Wienisch, M., Knöpfel, T., and Murthy, V.N. (2013). Distinct spatiotemporal activity in principal neurons of the mouse olfactory bulb in anesthetized and awake states. *Front. Neural Circuits* 7, 46.
- Brody, C.D., and Hopfield, J.J. (2003). Simple networks for spike-timing-based computation, with application to olfactory processing. *Neuron* 37, 843–852.

- Buzsáki, G., and Draguhn, A. (2004). Neuronal oscillations in cortical networks. *Science* 304, 1926–1929.
- Buzsáki, G., and Moser, E.I. (2013). Memory, navigation and theta rhythm in the hippocampal-entorhinal system. *Nat. Neurosci.* 16, 130–138.
- Carey, R.M., and Wachowiak, M. (2011). Effect of sniffing on the temporal structure of mitral/tufted cell output from the olfactory bulb. *J. Neurosci.* 31, 10615–10626.
- Carey, R.M., Verhagen, J.V., Wesson, D.W., Pérez, N., and Wachowiak, M. (2009). Temporal structure of receptor neuron input to the olfactory bulb imaged in behaving rats. *J. Neurophysiol.* 101, 1073–1088.
- Chen, X., Xia, Z., and Storm, D.R. (2012). Stimulation of electro-olfactogram responses in the main olfactory epithelia by airflow depends on the type 3 adenylyl cyclase. *J. Neurosci.* 32, 15769–15778.
- Chen, T.W., Wardill, T.J., Sun, Y., Pulver, S.R., Renninger, S.L., Baohan, A., Schreiter, E.R., Kerr, R.A., Orger, M.B., Jayaraman, V., et al. (2013). Ultrasensitive fluorescent proteins for imaging neuronal activity. *Nature* 499, 295–300.
- Cheung, M.C., Carey, R.M., and Wachowiak, M. (2009). A method for generating natural and user-defined sniffing patterns in anesthetized or reduced preparations. *Chem. Senses* 34, 63–76.
- Choi, G.B., Stettler, D.D., Kallman, B.R., Bhaskar, S.T., Fleischmann, A., and Axel, R. (2011). Driving opposing behaviors with ensembles of piriform neurons. *Cell* 146, 1004–1015.
- Connelly, T., Yu, Y., Grosmaire, X., Wang, J., Santarelli, L.C., Savigner, A., Qiao, X., Wang, Z., Storm, D.R., and Ma, M. (2015). G protein-coupled odorant receptors underlie mechanosensitivity in mammalian olfactory sensory neurons. *Proc. Natl. Acad. Sci. USA* 112, 590–595.
- Cury, K.M., and Uchida, N. (2010). Robust odor coding via inhalation-coupled transient activity in the mammalian olfactory bulb. *Neuron* 68, 570–585.
- Dana, H., Chen, T.W., Hu, A., Shields, B.C., Guo, C., Looger, L.L., Kim, D.S., and Svoboda, K. (2014). Thy1-GCaMP6 transgenic mice for neuronal population imaging in vivo. *PLoS ONE* 9, e108697.
- Franks, K.M., and Isaacson, J.S. (2006). Strong single-fiber sensory inputs to olfactory cortex: implications for olfactory coding. *Neuron* 49, 357–363.
- Friedrich, R.W. (2013). Neuronal computations in the olfactory system of zebrafish. *Annu. Rev. Neurosci.* 36, 383–402.
- Fukunaga, I., Herb, J.T., Kollo, M., Boyden, E.S., and Schaefer, A.T. (2014). Independent control of gamma and theta activity by distinct interneuron networks in the olfactory bulb. *Nat. Neurosci.* 17, 1208–1216.
- Grosmaire, X., Santarelli, L.C., Tan, J., Luo, M., and Ma, M. (2007). Dual functions of mammalian olfactory sensory neurons as odor detectors and mechanical sensors. *Nat. Neurosci.* 10, 348–354.
- Guo, Z.V., Hires, S.A., Li, N., O'Connor, D.H., Komiyama, T., Ophir, E., Huber, D., Bonardi, C., Morandell, K., Gutnisky, D., et al. (2014). Procedures for behavioral experiments in head-fixed mice. *PLoS ONE* 9, e88678.
- Haddad, R., Lanjuin, A., Madisen, L., Zeng, H., Murthy, V.N., and Uchida, N. (2013). Olfactory cortical neurons read out a relative time code in the olfactory bulb. *Nat. Neurosci.* 16, 949–957.
- Hayar, A., Shipley, M.T., and Ennis, M. (2005). Olfactory bulb external tufted cells are synchronized by multiple intraglomerular mechanisms. *J. Neurosci.* 25, 8197–8208.
- Hopfield, J.J. (1995). Pattern recognition computation using action potential timing for stimulus representation. *Nature* 376, 33–36.
- Huxter, J., Burgess, N., and O'Keefe, J. (2003). Independent rate and temporal coding in hippocampal pyramidal cells. *Nature* 425, 828–832.
- Imai, T. (2014). Construction of functional neuronal circuitry in the olfactory bulb. *Semin. Cell Dev. Biol.* 35, 180–188.
- Imai, T., Suzuki, M., and Sakano, H. (2006). Odorant receptor-derived cAMP signals direct axonal targeting. *Science* 314, 657–661.
- Kato, H.K., Chu, M.W., Isaacson, J.S., and Komiyama, T. (2012). Dynamic sensory representations in the olfactory bulb: modulation by wakefulness and experience. *Neuron* 76, 962–975.
- Kato, H.K., Gillet, S.N., Peters, A.J., Isaacson, J.S., and Komiyama, T. (2013). Parvalbumin-expressing interneurons linearly control olfactory bulb output. *Neuron* 80, 1218–1231.
- Kepecs, A., Uchida, N., and Mainen, Z.F. (2006). The sniff as a unit of olfactory processing. *Chem. Senses* 31, 167–179.
- Kepecs, A., Uchida, N., and Mainen, Z.F. (2007). Rapid and precise control of sniffing during olfactory discrimination in rats. *J. Neurophysiol.* 98, 205–213.
- Kleinfeld, D., and Deschênes, M. (2011). Neuronal basis for object location in the vibrissa scanning sensorimotor system. *Neuron* 72, 455–468.
- Kleinfeld, D., Deschênes, M., Wang, F., and Moore, J.D. (2014). More than a rhythm of life: breathing as a binder of orofacial sensation. *Nat. Neurosci.* 17, 647–651.
- Lalioti, M., and Heath, J. (2001). A new method for generating point mutations in bacterial artificial chromosomes by homologous recombination in *Escherichia coli*. *Nucleic Acids Res.* 29, E14.
- Laurent, G. (2002). Olfactory network dynamics and the coding of multidimensional signals. *Nat. Rev. Neurosci.* 3, 884–895.
- Macrides, F., and Chorover, S.L. (1972). Olfactory bulb units: activity correlated with inhalation cycles and odor quality. *Science* 175, 84–87.
- Margrie, T.W., and Schaefer, A.T. (2003). Theta oscillation coupled spike latencies yield computational vigour in a mammalian sensory system. *J. Physiol.* 546, 363–374.
- Mitra, P., and Bokil, H. (2008). *Observed Brain Dynamics* (New York: Oxford University Press).
- Miura, K., Mainen, Z.F., and Uchida, N. (2012). Odor representations in olfactory cortex: distributed rate coding and decorrelated population activity. *Neuron* 74, 1087–1098.
- Nagai, Y., Sano, H., and Yokoi, M. (2005). Transgenic expression of Cre recombinase in mitral/tufted cells of the olfactory bulb. *Genesis* 43, 12–16.
- Niessing, J., and Friedrich, R.W. (2010). Olfactory pattern classification by discrete neuronal network states. *Nature* 465, 47–52.
- Oka, Y., Takai, Y., and Touhara, K. (2009). Nasal airflow rate affects the sensitivity and pattern of glomerular odorant responses in the mouse olfactory bulb. *J. Neurosci.* 29, 12070–12078.
- Panzeri, S., Brunel, N., Logothetis, N.K., and Kayser, C. (2010). Sensory neural codes using multiplexed temporal scales. *Trends Neurosci.* 33, 111–120.
- Schaefer, A.T., Angelo, K., Spors, H., and Margrie, T.W. (2006). Neuronal oscillations enhance stimulus discrimination by ensuring action potential precision. *PLoS Biol.* 4, e163.
- Schoppa, N.E. (2006). Synchronization of olfactory bulb mitral cells by precisely timed inhibitory inputs. *Neuron* 49, 271–283.
- Schoppa, N.E., and Westbrook, G.L. (2001). Glomerulus-specific synchronization of mitral cells in the olfactory bulb. *Neuron* 31, 639–651.
- Severson, K.S., Xu, D., Van de Loo, M., Bai, L., Ginty, D.D., and O'Connor, D.H. (2017). Active touch and self-motion encoding by merkel cell-associated afferents. *Neuron* 94, 666–676.e9.
- Shusterman, R., Smear, M.C., Koulakov, A.A., and Rinberg, D. (2011). Precise olfactory responses tile the sniff cycle. *Nat. Neurosci.* 14, 1039–1044.
- Sirotin, Y.B., Shusterman, R., and Rinberg, D. (2015). Neural coding of perceived odor intensity. *eNeuro* 2, <https://doi.org/10.1523/ENEURO.0083-15.2015>.
- Smear, M., Shusterman, R., O'Connor, R., Bozza, T., and Rinberg, D. (2011). Perception of sniff phase in mouse olfaction. *Nature* 479, 397–400.
- Smear, M., Resulaj, A., Zhang, J., Bozza, T., and Rinberg, D. (2013). Multiple perceptible signals from a single olfactory glomerulus. *Nat. Neurosci.* 16, 1687–1691.
- Spors, H., and Grinvald, A. (2002). Spatio-temporal dynamics of odor representations in the mammalian olfactory bulb. *Neuron* 34, 301–315.

- Spors, H., Wachowiak, M., Cohen, L.B., and Friedrich, R.W. (2006). Temporal dynamics and latency patterns of receptor neuron input to the olfactory bulb. *J. Neurosci.* 26, 1247–1259.
- Stopfer, M., Jayaraman, V., and Laurent, G. (2003). Intensity versus identity coding in an olfactory system. *Neuron* 39, 991–1004.
- Thévenaz, P., Ruttimann, U.E., and Unser, M. (1998). A pyramid approach to subpixel registration based on intensity. *IEEE Trans. Image Process.* 7, 27–41.
- Tian, L., Hires, S.A., Mao, T., Huber, D., Chiappe, M.E., Chalasani, S.H., Petreanu, L., Akerboom, J., McKinney, S.A., Schreiter, E.R., et al. (2009). Imaging neural activity in worms, flies and mice with improved GCaMP calcium indicators. *Nat. Methods* 6, 875–881.
- Uchida, N., and Mainen, Z.F. (2003). Speed and accuracy of olfactory discrimination in the rat. *Nat. Neurosci.* 6, 1224–1229.
- Uchida, N., Poo, C., and Haddad, R. (2014). Coding and transformations in the olfactory system. *Annu. Rev. Neurosci.* 37, 363–385.
- Verhagen, J.V., Wesson, D.W., Netoff, T.I., White, J.A., and Wachowiak, M. (2007). Sniffing controls an adaptive filter of sensory input to the olfactory bulb. *Nat. Neurosci.* 10, 631–639.
- Wachowiak, M., Economo, M.N., Díaz-Quesada, M., Brunert, D., Wesson, D.W., White, J.A., and Rothermel, M. (2013). Optical dissection of odor information processing *in vivo* using GCaMPs expressed in specified cell types of the olfactory bulb. *J. Neurosci.* 33, 5285–5300.
- Wellis, D.P., Scott, J.W., and Harrison, T.A. (1989). Discrimination among odorants by single neurons of the rat olfactory bulb. *J. Neurophysiol.* 61, 1161–1177.
- Wilson, R.I., and Mainen, Z.F. (2006). Early events in olfactory processing. *Annu. Rev. Neurosci.* 29, 163–201.
- Zariwala, H.A., Borghuis, B.G., Hoogland, T.M., Madisen, L., Tian, L., De Zeeuw, C.I., Zeng, H., Looger, L.L., Svoboda, K., and Chen, T.W. (2012). A Cre-dependent GCaMP3 reporter mouse for neuronal imaging *in vivo*. *J. Neurosci.* 32, 3131–3141.

STAR★METHODS**KEY RESOURCES TABLE**

REAGENT or RESOURCE	SOURCE	IDENTIFIER
Antibodies		
Goat anti-NQO1	Abcam	Cat# ab2346; RRID: AB_302995
Rabbit anti-GFP	Thermo Fisher	Cat# A11122; RRID: AB_221569
Chicken anti-GFP	Aves Labs	Cat# GFP-1010; RRID: AB_2307313
Goat anti-OMP	Wako	Cat# 019-22291; RRID: AB_664696
Mouse anti-GAD65	Abcam	Cat# ab26113; RRID: AB_448989
Mouse anti-GAD67	Millipore	Cat# MAB5406; RRID: AB_2278725
Mouse anti-Reelin	Millipore	Cat# MAB5364; RRID: AB_2179313
Chemicals, Peptides, and Recombinant Proteins		
p-Anisaldehyde	Nacalai	Cat# 03007-82
Anisol	Nacalai	Cat# 03025-42
Benzaldehyde	Nacalai	Cat# 04006-62
Cineole	Nacalai	Cat# 09042-32
trans-Cinnamaldehyde	Nacalai	Cat# 09024-72
Citral	Nacalai	Cat# 09103-32
Enanthaldehyde	Nacalai	Cat# 14333-62
Eugenol	Nacalai	Cat# 15806-42
n-Hexylaldehyde	Nacalai	Cat# 18029-42
n-Octylamine	Nacalai	Cat# 25512-72
Phenethylamine	Nacalai	Cat# 27125-92
Propionaldehyde	Nacalai	Cat# 29015-56
Triethylamine	Nacalai	Cat# 34805-62
n-Valeraldehyde	Nacalai	Cat# 36011-92
Butyric acid	TCI	Cat# B0754
S-(+)-Carvone	TCI	Cat# C0704
β-Citronellol	TCI	Cat# C0370
Ethylhexanoate	TCI	Cat# H0108
(+)-Fenchone	TCI	Cat# F0163
Hexanoic acid	TCI	Cat# H0105
(+)-Limonene	TCI	Cat# L0047
2-Nonanone	TCI	Cat# N0293
Acetophenone	Wako	Cat# 014-00423
n-Amyl acetate	Wako	Cat# 018-03623
(Z)-Jasmone	Wako	Cat# 14333-62
Guaiacol	Wako	Cat# 133-08302
Methyl benzoate	Wako	Cat# 132-01993
DAPI solution	Thermo Fisher	Cat# 62248
Critical Commercial Assays		
Antigen Retrieval Solution High pH	Dako	Cat# S2368
Deposited Data		
Raw image data	This paper	http://ssbd.qbic.riken.jp/set/20171001/
Experimental Models: Organisms/Strains		
OMP-tTA (C57BL/6N-Tg(OMP-tTA)3Tima)	This paper	Accession# CDB0506T; MGI:5922006
TRE-GCaMP3 (C57BL/6N-Tg(tetO-GCaMP3)2Tima)	This paper	Accession# CDB0505T; MGI:5922007

(Continued on next page)

Continued

REAGENT or RESOURCE	SOURCE	IDENTIFIER
Pcdh21-Cre (C57BL/6Cr-Tg(Pcdh21-cre)BYoko)	RIKEN BRC	Cat# RBRC02189; RRID: IMSR_RBRC02189
Ai38 (B6;129S-Gt(ROSA)26Sor ^{tm3(CAG-GCaMP3)Hze} /J)	The Jackson Laboratory	Cat# JAX:014538; RRID: IMSR_JAX:014538
C57BL/6J-Tg(Thy1-GCaMP6f)GP5.11Dkim/J	The Jackson Laboratory	Cat# JAX:024339; RRID: IMSR_JAX: 024339
I7-ires-gap-CFP (C57BL/6-Tg(Olfr16-Olr226-ECFP)1Hsak)	RIKEN BRC	Cat# RBRC02931; RRID: IMSR_RBRC02931
Oligonucleotides		
OMP-tTA genotyping primer, forward: TCACCCCTCCAGCCTGCCTAC	This paper	N/A
OMP-tTA genotyping primer, reverse: CGTCGCGATGTGAGAGGAGA	This paper	N/A
TRE-GCaMP3 genotyping primer, forward: AACCGTCAGATCGCCTGGAG	This paper	N/A
TRE-GCaMP3 genotyping primer, reverse: CGGTACCGCCCTTGACAGC	This paper	N/A
Pcdh21-Cre genotyping primer, forward: TGCCACCAGCCAGCTATCAA	This paper	N/A
Pcdh21-Cre genotyping primer, reverse: TGAGGGTCCATGGTGATACAAGG	This paper	N/A
Ai38 genotyping primer, forward: CACACCTCCCCCTGAACCTG	This paper	N/A
Ai38 genotyping primer, reverse: CGCCTTGATGCCGTTCTTCT	This paper	N/A
Thy1-GCaMP6f genotyping primer, forward: CTGACTGAAGAGCAGATCGCAGAAT	This paper	N/A
Thy1-GCaMP6f genotyping primer, reverse: GCAGCGTATCCACATAGCGTAAAG	This paper	N/A
Recombinant DNA		
pTet-Off Advanced	Clontech	Cat# 631070
pTRE-Tight	Clontech	Cat# 631059
BAC clone RP24-221I11	BACPAC Resources Center	Cat# RP24-221I11
BAC clone RP23-401D9	BACPAC Resources Center	Cat# RP23-401D9
GCaMP3	Tian et al., 2009	Addgene Plasmid #22692
pAAV-EF1a-mCherry-IRES-WGA-Cre	Laboratory of K. Deisseroth	N/A
pKOV-KanF	Laliovi and Heath, 2001	N/A
Software and Algorithms		
MATLAB	MathWorks	RRID: SCR_001622
Chronux	http://chronux.org	RRID: SCR_005547
ImageJ	https://imagej.nih.gov/ij/	RRID: SCR_003070
Cell Magic Wand plugin	https://www.maxplanckflorida.org/fitzpatricklab/software/cellMagicWand/	N/A
Other		
Insight DS Dual	Spectra-Physics	N/A
FV1000MPE	Olympus	N/A
XLPLN25XWMP	Olympus	N/A
Type T Thermocouple Probe	Physitemp	Cat# IT-23
T-type Pod	AD Instruments	Cat# ML312
PowerLab 4/26	AD Instruments	Cat# ML846
Heating Pad System for Rodents FHC-HPS	FHC	FHC-HPS
Olfactometer	Technica / Matsumi Kagaku Keisoku	N/A

CONTACT FOR REAGENT AND RESOURCE SHARING

Further information and requests for resources and reagents should be directed to and will be fulfilled by the Lead Contact, Takeshi Imai (t-imai@med.kyushu-u.ac.jp).

EXPERIMENTAL MODEL AND SUBJECT DETAILS

Mice

All animal experiments were approved by the Institutional Animal Care and Use Committee (IACUC) of the RIKEN Kobe Branch. *OMP-tTA* (line #3; Accession number CDB0506T: <http://www2.clst.riken.jp/arg/TG%20mutant%20mice%20list.html>; MGI:5922006) crossed to *TRE-GCaMP3* mice (high copy line; Accession number CDB0505T; MGI:5922007), *Pcdh21-Cre* (RIKEN BRC, RBRC02189) (Nagai et al., 2005) crossed to *Ai38* mice (*Rosa26-CAG-LSL-GCaMP3*, JAX#014538 from Jackson laboratory) (Zariwala et al., 2012), and *Thy1-GCaMP6f* mice (JAX# 024339) (Dana et al., 2014) were used for *in vivo* calcium imaging. *I7-ires-gap-CFP* (under *MOR23* promoter) mouse (RBRC02931) (Imai et al., 2006) was obtained from RIKEN BRC. The *BAC* (*bacterial artificial chromosome*)-*OMP-tTA* construct was generated by inserting the *tTA-Advanced-SV40 poly A signal* cassette from *pTet-Off Advanced* (Clontech) to the start codon of the *OMP* gene in the ~200kb *BAC* clone RP24-221111 (BACPAC; Figure S1A). The *tTA-polyA* cassette (1.2kb) was fused with the PCR-generated homologous flanking sequences of the *OMP*, subcloned in *pKOV-KanF*, and was used for homologous recombination in *E. coli* carrying RP24-221111 as described previously (Lalioti and Heath, 2001). For the generation of the *TRE-GCaMP3* construct, a *TRE* (Tet response element; 318bp) from *pTRE-Tight* (Clontech), a *GCaMP3* coding sequence (1353bp), a *WPRE* (609bp), and a *SV40 poly A signal* (189bp) from *pTRE-Tight* were inserted into a PCR-generated *ROSA26* intron sequences and then subcloned into *pKOV-KanF* for homologous recombination in *E. coli* carrying the ~200kb *BAC* clone RP23-401D9 (BACPAC; Figure S1B). *GCaMP3* sequence (Addgene #22692) and *pAAV-EF1a-mCherry-IRES-WGA-Cre* for *WPRE* were kindly provided by L. Looger (Janelia Farm) and K. Deisseroth (Stanford University), respectively. The *BAC* DNA was purified with plasmid midi-prep kit (MACHEREY-NAGEL). The vector sequences were removed by restriction enzyme digestions (*Ascl*) and purified with Amicon Ultra-4 (Millipore). DNA constructs were microinjected into pronuclei of C57BL/6N fertilized eggs. Genotyping primers were 5'-TCACCCCTCCAGCCTGCCTAC-3' and 5'-CGTCGCGATGTGAGAGGAGA-3' for *OMP-tTA* mice; 5'-AACCGTCAGATGCCCTGGAG-3' and 5'-CGGTACGCCCTTGACAGC-3' for *TRE-GCaMP3* mice (the primer sites are indicated in Figures S1A and S1B). We established 3 transgenic lines for *OMP-tTA* and 2 transgenic lines for *TRE-GCaMP*, but used only one combination showing highest expression levels of *GCaMP3*. Some offspring of *Pcdh21-Cre*; *Ai38* showed *GCaMP3* expression throughout the brain likely due to leaky expression of Cre in early development, and these samples were not used for imaging experiments. *Ai38* was in a 129/C57BL/6 mixed background and all other lines were in a C57BL/6 background. *M/T-GCaMP6f* (*Thy1-GCaMP6f*, GP5.11) mice were used in Figures 3, 4B, 7, 8, S3C–S3G, S7, and S8. All other imaging experiments for M/T cells were performed in *M/T-GCaMP3* (*Pcdh21-Cre*; *Ai38*) mice. *GCaMP3* signals have been demonstrated to reliably report spikes in M/T cells both in somata and dendrites (Kato et al., 2012; Wachowiak et al., 2013).

METHOD DETAILS

Immunohistochemistry

Immunohistochemistry was performed with standard techniques. Cryostat sections were prepared at 18 µm thick. Sections were pretreated with 4% PFA in PBS, and 5% Donkey serum (Jackson) in PBS with 0.1% Triton X-100. Goat anti-NQO1 (Abcam, ab2346), rabbit anti-GFP (Thermo Fisher, A11122), chicken anti-GFP (Aves, GFP-1010), goat anti-OMP (Wako, 019-22291), mouse anti-GAD65 (Abcam, ab26113), mouse anti-GAD67 (Millipore, MAB5406), and mouse anti-Reelin (Millipore, MAB5364) antibodies were used at 1:100, 1:200, 1:200 1:1000, 1:500, 1:500, and 1:100 dilutions, respectively. Alexa Fluor 488, 555, or 647 conjugated secondary antibodies (Thermo Fisher, A11039, A21206, A21432, A21449, A31570, and A31572) were used at 1:200 dilutions. Sections were counterstained with DAPI (Thermo Fisher). Immunostaining with anti-NQO1 and anti-Reelin antibodies was preceded by antigen retrieval in Antigen Retrieval Solution High pH (Dako, S2368) at 65°C for 1 hr and in citrate buffer pH 6.0 at 120°C for 15 min, respectively.

Two-photon imaging

In vivo imaging was performed in male mice (8–16 weeks of age), which were awake or anesthetized with ketamine/xylazine (80 mg/kg and 16 mg/kg, respectively). During surgery and imaging, the depth of anesthesia was assessed by the toe-pinch reflexes, and supplemental doses were added when necessary. For imaging of the OB, a craniotomy 2–3 mm in diameter was made over the right dorsal OB leaving the dura mater intact. The dura was covered with a thin layer of silicone sealant (Kwik-Sil, WPI) and a 4 mm diameter circular coverslip (Matsunami), which was secured with super-glue and dental cement (Shofu). The dorsal zone of the OE was imaged through the nasal bone, which was thinned by a dental drill. OSNs in this area project axons to the dorsal domain of OB, where *in vivo* imaging of OB was performed. Anesthetized mice were head-fixed under a microscope using a custom-designed stage with ear-bars (Muromachi). The body temperature was maintained at ~37°C using a heating pad (FHC, FHC-HPS).

For imaging in awake animals, a custom aluminum head bar (4×22 mm) for head-fixation was glued to the skull behind the cranial window. Water-restriction was started 2-3 days after surgery (Guo et al., 2014). Mice under water-restriction were acclimated to head-fixation in an acrylic tube, and then to a custom-made circular treadmill (running wheel) for 10-15 days, 30 min each. Imaging sessions were performed on the running wheel as high-frequency sniffing was more frequently observed on the running wheel than in the acrylic tube. During imaging sessions, mice showed little signs of distress.

GCAMP3 and GCAMP6f were excited at 920 nm (Spectra-Physics, Insight DS Dual), and images were acquired with an upright two-photon laser-scanning microscope (Olympus, FV1000MPE) using a water-immersion 25x objective lens (Olympus, XLPLN25XWMP) at ~ 2 Hz for full-field images and at 20~30 Hz for high-speed imaging (clip scan mode). Typically 30-50 and 4-6 glomeruli were imaged in a full-field image and a clip-scan image, respectively.

Measurement of sniff cycles

Sniff cycles under freely-breathing conditions were monitored with a thermocouple (Physitemp, IT-23) (Kepcs et al., 2007). For anesthetized mice, the tip of the thermocouple was placed at the opening of the left nostril, which was contralateral to the imaged side, using a micromanipulator (Narishige). For awake mice, a 7-mm-long stainless intranasal cannula (Medical-pipe, inside diameter 0.4 mm / outside diameter 0.7 mm) was chronically implanted into the dorsal recess of the left nostril (Cheung et al., 2009), and thermocouple was inserted into the cannula during imaging. The temperature signal was amplified with a signal conditioner (AD Instruments, ML312), and recorded at 1 kHz using PowerLab (AD Instruments). To remove slow baseline drift and electromagnetic interference from nearby electronics, temperature signals were filtered for the 0.5-40 Hz band. The sniff timing was determined by the local temperature minima in anesthetized mice and local temperature maxima in awake mice, which were the most reliable indicators for sniff cycles in each condition (Figures 2A and 3E).

Tracheotomy and artificial sniffing

In experiments using artificial sniffing, the trachea was doubly cut and inserted with two silicone tubes (inside diameter 0.5 mm) (Oka et al., 2009). Mice freely breathed through the lower tube. The inserted end of the upper tracheotomy tube was positioned to the nasopharynx, and the other end was connected to a solenoid valve, a flow meter, and an air suction pump in all the experiments except Figure 3. Mispositioning of the inserted tube end led to weak and unstable suctioning, and these samples were not used for imaging experiments. Unless otherwise noted, the nasal airflow rate was 200 ml/min and the durations of negative pressure pulses were 300 ms ON / 300 ms OFF (1 cycle = 600 ms). The solenoid valves for nasal airflow and odor delivery were regulated through relay circuits and the computer programs were written in Microsoft Visual Studio.

For artificial sniffing at 1-12 Hz with a custom syringe pump (Figure 3), the tracheotomy tube was connected to a 3 mL glass syringe (Tsubasa Industry, Numbered syringe 3cc) driven by a solenoid actuator (Takaha, CA1578) (Cheung et al., 2009). The working volume of this syringe pump was adjusted to 0.5 mL / stroke. Mean oscillation traces and power spectra for artificial sniffing at 1, 2, 4, 6, 8, 10 and 12 Hz were respectively obtained from 20 s imaging sessions.

In vivo Ca²⁺ imaging

For two-photon Ca²⁺ imaging, clean air filtered through activated charcoal was continuously delivered to the nose. Anesthetized mice were carefully and firmly fixed under a microscope to avoid motion by respiration and pulsation. To block the nasal airflow (Figures 2A and 2B), the right nostril (ipsilateral to the imaged OB) was completely sealed with silicone adhesive (WPI, Kwik-Sil).

To determine oscillation phases for a large number of glomeruli in the dorsal OB (Figure 2D), each of the 7 full-field image areas ($500 \mu\text{m} \times 500 \mu\text{m}$, 256 × 256 pixel) was divided into 9 horizontal strips. They were sequentially analyzed by high-speed imaging for 6 s and were used to determine oscillation phases.

Odor stimulations

Odorants were diluted in 1 mL of mineral oil in a 50 mL vial, and saturated odor vapor was further diluted ($10 \times$) to the indicated nominal concentrations with filtered air using a custom-made olfactometer (Technica / Matsumi Kagaku Keisoku). Diluted odors were delivered at 0.5 - 1 L/min except in Figures 7, 8, S7, and S8, where the diluted odor was delivered at 2 l/min to ensure a rapid exchange between odors and filtered air (Figure S7A). Only for the experiments in Figure 6, saturated odor vapors were directly used without further dilution in clean air. In experiments combining artificial sniffing and odor stimulations, odor stimuli were applied more than 40 s after starting artificial sniffing, and were provided for 6-12 s. Inter-trial intervals were 2-3 min. Odorants were purchased from Tokyo Kasei, Nacalai Tesque, or Sigma Aldrich and stored at 4°C. Odorants were diluted just prior to use. Abbreviations: Aa, amylacetate; AcP, acetophenone; BuA, butyric acid; Bz, benzaldehyde; Ehx, ethylhexanoate; Gua, guaiacol; Hex, hexanoic acid; Oca, octylamine; Pna, phenethylamine; Val, valeraldehyde.

QUANTIFICATION AND STATISTICAL ANALYSIS

Image analysis

Mechanical lateral drift in the time-lapse imaging data was corrected using the TurboReg plug-in in ImageJ v1.46 (<https://imagej.nih.gov/ij/>) when necessary (Thévenaz et al., 1998). ROIs were manually determined for individual glomeruli with ImageJ. ROIs for

individual somata were semi-automatically determined using the Cell Magic Wand plugin. Fluorescence intensity data were analyzed by custom-written codes in MATLAB (MathWorks) software. For analysis in Figures 2, 3, and S2A–S2D changes in fluorescence intensity (ΔF) were normalized to the mean intensity over the whole imaging period (F). In all other experiments, the ΔF was normalized to the mean intensity for 6 s before stimulus onset (F_0), and, unless otherwise noted, the response amplitude was defined as the mean $\Delta F/F_0$ during the first 3 s after stimulus onset. We used the mean $\Delta F/F_0$ rather than peak $\Delta F/F_0$, since the peak $\Delta F/F_0$ for oscillating glomeruli will always have a positive value even without stimulus. To analyze temporal activity patterns (for most experiments in this study) time vectors for individual ROIs were corrected for the scanning delay, based on the ROI centroid position. The correction of the timing was small (differences among ROIs < 10 ms) except for Figures S2A–S2D (up to ~100 ms).

Oscillation analysis

The oscillation phase was determined as latency from cycle onset (sniff timing) to the half-rise timing of GCaMP3 and GCaMP6 fluorescence. Fluorescence rise time (τ_{on}) of GCaMP3 and GCaMP6f upon action potentials is fast and constant across a wide range of firing rates, whereas decay time (τ_{off}) is slow and strongly affected by the firing rate (Chen et al., 2013; Wachowiak et al., 2013). Thus, the half-rise timing can be best used to estimate the timing of burst firing. The sniff timing was defined by the suction onset (electrical signals to the solenoid valve) in artificial sniffing.

To reliably determine the half-rise timing, we used mean oscillation traces of fluorescence intensity across multiple cycles or trials. To analyze spontaneous oscillations in freely breathing anesthetized mice in Figures 2C and S2A–S2D, mean oscillation traces were obtained by averaging more than 300 sniff cycles during 2 min imaging sessions.

To analyze spontaneous oscillations in freely breathing, awake running mice (Figures 3D–3I), mean oscillation traces for different sniff frequency ranges (1-2, 2-3, 3-4, 4-5, 5-6, 6-8, 8-10 and 10-12 Hz) were obtained by averaging more than 20 sniff cycles in each frequency range during 8 min imaging sessions. If sniff events in the frequency range occurred more than 20 times during the 8 min imaging sessions, the half-rise timing was determined from the oscillatory rise (from local minimum [L_{min}] to local maximum [L_{max}]) of the mean traces, if L_{min} occurred between 50–180 ms after inhalation onset, and if L_{max} occurred within 200 ms after L_{min} . These requirements were used to exclude traces where half-rise could not be determined because rises in sequential two sniff cycles are continuous without decay typically during high-frequency sniffing (> 10 Hz).

In odor stimulations using freely breathing, awake running mice (Figures 4B and S3D), odor exposure for 10 s was repeated every 1 min for 10 times. Mean oscillation traces for pre-odor and odor periods were obtained by analyzing respective 10 s (total 100 s each) periods.

In odor or airflow stimulations in tracheotomized mice (Figures 4C–4G and S2E–S2H), mean oscillation traces were determined for pre-stimulus periods (6 s) and odor-stimulation period by cycle averaging (6 s for Figures 4C–4G and 3 s for Figures S2E–S2H). Then, we considered rise and fall amplitude in the mean traces: for pre-stimulus traces, half-rise phase (θ_0) was determined if the rise amplitude was larger than 2% $\Delta F/F_0$; for traces after stimulus onset, half-rise phase (θ_{stim}) was determined if the rise amplitude and fall amplitude were larger than 5% and 1%, respectively. The threshold for the fall amplitude was required to exclude non-oscillatory monotonically-increasing responses. Inhibitory responses typically dampened oscillations and tended to be excluded from our analysis. Oscillation phase shifts were calculated as $\theta_{stim} - \theta_0$.

To analyze oscillation phases in individual cycles after odor onset (Figures 5, 8, and S5), mean traces across five (Figures 5 and S5) or two (Figure 8) trials were used to determine the half-rise phase of each cycle (θ_{stim}). From the mean traces, all the local maxima (L_{max}) and local minima (L_{min}) were identified using a 100-ms time window. Then, for every set of three successive local extreme values ($L_{min} - L_{max} - L_{min}$), the half-rise phase was determined if the rise amplitude and fall amplitude were larger than 5% and 1% $\Delta F/F_0$, respectively. When half-rise phase was not assigned to any one of the cycles, the data were excluded from further analysis (see below for the sample size information). In rare cases, multiple half-rise events were detected in a cycle; in that case, the earliest half-rise phase in the cycle was adopted as the oscillation phase. Oscillation phase shifts were calculated as $\theta_{stim} - \theta_0$, where θ_0 was determined from mean oscillation traces across 10 sniff cycles before the stimulus onset.

Power spectral analysis of sniff-coupled activity

For spectral analysis, power spectral densities were estimated by the multi-taper method implemented in the Chronux toolbox (<http://chronux.org/>) (Mitra and Bokil, 2008) with the bandwidth parameter NW = 4 and the number of tapers K = 5 (Figure 2B), or NW = 2 and K = 3 (Figure 3C).

Responses to airflow changes versus odor stimuli

For analysis in Figures 4C–4F, single-trial responses were obtained for odor stimuli (Bz or Aa diluted at 1:1000) and respiratory changes in 387 glomeruli from 11 mice. The two trials (airflow changes versus one of the two odors) were performed in succession for the same image area. Data for the two odors were combined in this analysis. See the **oscillation analysis** section for how to determine the oscillation phase shifts. Oscillation phases for airflow changes and odor stimuli were analyzed in 291 and 264 glomerulus-stimulus pairs, respectively, out of 387 pairs in total (75% and 68%).

Temporal dynamics of the population odor responses

To analyze the ensemble rate code for 27 odorants (Figure S4), imaging trials with a low frame rate (0.429 s/frame) were repeated three times (a single mouse for each odor, $n = 6$ mice for total 27 odors). For glomeruli whose response peaks exceeded 40% $\Delta F/F_0$, the mean activity time series across three trials were shown in heatmaps (Figure S4A), and Spearman's correlation coefficients to the 1st frame after odor onset (reference) were calculated for each frame (Figure S4B).

To compare the stability of rate code and phase code (Figures 5 and S5), we first performed single full-field imaging at a low frame rate (0.429 s/frame). Then, glomeruli whose response peaks exceeded 40% $\Delta F/F_0$ were identified using custom-written macros in ImageJ v1.46. These glomeruli were then analyzed in several groups to limit y pixel size of the imaging field for high-speed imaging. For each group, high-speed imaging (clip scan, 25–40 ms/frame) were repeated five times. Using trial-averaged traces, the pre-stimulation phase (θ_0) was determined from cycle-averaged mean traces of the 10 cycles before stimulus onset. See [oscillation analysis](#) section for determination of oscillation phases in individual sniff cycles during odor periods (θ_{stim}). Oscillation phase shifts (phase code) were calculated as $\theta_{stim} - \theta_0$, and rate code was obtained by calculating the mean $\Delta F/F_0$ in each sniff cycle. Odor concentrations were 1:1000 for phenethylamine, propionaldehyde, p-anisaldehyde, trans-cinnamaldehyde, S-(+)-carvone, guaiacol, and eugenol; and 1:100 for the others. The sample sizes were $n = 12/33$ (Oca; the number of glomeruli whose oscillation phase were determined for all of the 20 sniff cycles, over the total number including the remaining glomeruli; $n = 3$ mice), and 33/45 (Val, $n = 3$ mice), 21/28 glomeruli (Bua, $n = 2$ mice), 16/21 (Hex, $n = 2$ mice), 20/30 (Ehx, $n = 2$ mice), 14/25 (Bz, $n = 2$ mice), 21/32 (Gua, $n = 2$ mice), 21/33 (Acp, $n = 2$ mice).

Rate- and phase- representations of odor concentrations

For analysis in Figures 6 and S6, single-trial responses were imaged for serially-diluted odors. Odorants were diluted in mineral oil at 1:100–1:8100, and the saturated odor vapor was directly used without further dilution in the clean air. Pure mineral oil without odorants was used in blank trials. Among the tested 14 odors, 10 odors were pure odorants, and the other 4 odors were binary mixtures of odorants. The 14 odors were paired into 7 groups, and a pair of odors was tested for the same glomerular set in each experiment.

To analyze the effects of odor concentrations on rate code (mean response amplitude during 6 s odor exposure) and phase code, we considered glomeruli whose response peaks exceeded 40% $\Delta F/F_0$ in at least one of the five concentrations (dataset 1). From this dataset, we then considered glomeruli whose oscillation phase could be determined for all of the five concentration conditions (dataset 2; see the [oscillation analysis](#) section for the determination of oscillation phase). Most of the analyses were performed using dataset 2, and dataset 1 was used for correlation analysis on rate code in Figure S6C (rate code in all). Both datasets resulted in similar concentration-dependent changes in rate code. The dataset size (numbers of glomeruli in dataset 2 / dataset 1) was $n = 17/23$ (Aa, $n = 3$ mice), 18/19 (Ehx, $n = 3$ mice), 20/27 (Val, $n = 2$ mice), 20/31 (Bz, $n = 2$ mice), 21/28 (Acp, $n = 4$ mice), 25/29 (Gua, $n = 4$ mice), 24/33 (Bua, $n = 2$ mice), 19/19 (Hex, $n = 2$ mice), 24/27 (Oca, $n = 5$ mice), 14/15 (Pna, $n = 5$ mice), 15/25 (binary mixture ratio, Bz:Val = 7:3, $n = 2$ mice), 22/28 (Bz:Val = 3:7, $n = 2$ mice), 19/25 (Acp:Gua = 7:3, $n = 2$ mice) and 18/25 (Acp:Gua = 3:7, $n = 2$ mice).

Classification analysis

Odor classification analysis was performed for the 7 pairs of odors using a Euclidean distance-based classifier (Kato et al., 2012; Stopfer et al., 2003) (Figures 6D and S6D) or a support vector machine (SVM) classifier (Cury and Uchida, 2010) with a linear kernel (Figure S6E). For each pair, we considered glomeruli where (1) their response peaks exceeded 40% $\Delta F/F_0$ in at least one of the 10 conditions (5 conc. \times 2 odors) and (2) their oscillation phase could be determined for all of the 10 conditions. The number of glomeruli satisfying these two criteria was 12 (Aa versus Ehx), 16 (Val versus Bz), 19 (Acp versus Gua), 18 (Bua versus Hex), 17 (Oca versus Pna), 17 (binary mixture ratio, Bz:Val = 7:3 versus 3:7), and 17 (Acp:Gua = 7:3 versus 3:7). Classification between two odors was repeated with random combinations of glomeruli from the dataset (number of glomeruli, $N_{glom} = 1, 2, 3, 4$, and 5); information of each odor is expressed by either its rate code (mean $\Delta F/F_0$ during odor stimulation) or its phase code (oscillation phase) as an $N_{glom} \times 5$ (number of conc.) matrix. Among the 10 conditions (5 conc. \times 2 odors), one (Figure 6D) or two (Figures S6D and S6E) concentrations were randomly chosen for references (1 conc. \times 2 odors, 2 conditions; or 2 conc. \times 2 odors, 4 conditions), and the remaining conditions (4 conc. \times 2 odors, 8 conditions; or 3 conc. \times 2 odors, 6 conditions) were used as a test set. When a classifier based on the Euclidean distance was used, we calculated the Euclidean distance between a test condition (a vector of N_{glom} dimensions) and the reference conditions (2 vectors of N_{glom} dimensions); when two concentrations were used as the reference sets, we calculated the mean vector of the two concentrations for each odor. If the test vector is closest to a vector of the same odor, the classification was considered to be correct. The classification was repeated 50,000 times to obtain mean correct classification rates. Classification using a SVM classifier was performed following the same procedure.

Odor responses in the presence and absence of mechanosensory oscillations

To examine odor responses in m+ and m– conditions (Figures 7 and S7), an odor (Aa, Bz, or Val diluted at 1:1,000, 1:10,000 and 1:100,000) was applied for 1.2 s (two sniff cycles). Odor trials were repeated 6 times with 1-min intervals. Response half-rise timing and amplitude were quantified for trial-averaged traces. The response amplitude was defined as the mean amplitude in the 1st sniff cycle in $n = 115$ glomerulus-odor pairs for odor dilutions at 1:1,000 ($n = 29, 34$ and 52 for Aa, Bz and Val, respectively, from $n = 4$ mice); $n = 132$ pairs for 1:10,000 ($n = 33, 52, 47$ from $n = 3$ mice); $n = 114$ pairs for 1:100,000 ($n = 43, 35, 36$ from $n = 3$ mice). Response

half-rise timing was defined as the time taken to reach the half-rise point of the 1st sniff cycle for glomerulus-odor pairs whose response peak was (1) larger than 40% $\Delta F/F_0$ and (2) reached the peak in the 1st cycle in both m+ and m- conditions: n = 79 pairs for 1:1,000; n = 80 pairs for odor dilutions at 1:10,000; n = 61 pairs for 1:100,000. To evaluate variability across trials (half-rise SD and peak SD), the half-rise timing and peak amplitudes in the 1st cycle were determined for each trial to obtain a standard deviation in glomerulus-odor pairs which met the above two requirements in all of 12 trials (6 trials each for m+ and m-): n = 66 pairs for odor dilutions at 1:1,000; n = 76 pairs for 1:10,000; n = 56 pairs for 1:100,000.

For odor classification by single-trial phase code (response half-rise timing) in Figures 7D and S7E, additional experiments were performed using two pairs of odorant mixtures with different ratios 7:3 and 3:7 (total concentrations were 1:100,000 for mixtures of Aa and Val; 1:10,000 for mixtures of Bz and Ehx), repeating 6 odor trials in m+ and m- for each odor. The half-rise timing in each trial was determined for glomeruli where the two requirements (response peak is reached within the 1st cycle; peak amplitude $\geq 40\% \Delta F/F_0$) were met in all of 24 trials (6 trials each for m+ and m- in two odors): n = 22 from total imaged 66 glomeruli for Aa and Val mixtures (n = 2 mice); n = 19 from total 45 glomeruli for Bz and Ehx mixtures (n = 1 mouse). Classification between two odors was repeated with all the possible combinations of 1-5 glomeruli (22-26,334 combinations for Aa and Val mixtures; 19-11,628 combinations for Bz and Ehx mixtures). From the total 6 trials, the phase code in one trial was used as reference, and the remaining trials were used as a test set. The test set was classified between two odors based on the Euclidean distance: if the test set is closest to reference of the same odor, the classification was considered to be correct. The classification was repeated for all the combinations of reference and test sets.

For quantifying the oscillation phase in each odor cycle (Figure 8), 4 odors (Acp, Bz, and Val diluted at 1:100, and Gua diluted at 1:1000) were paired into 2 groups, and each pair of odors was tested for the same glomeruli set in each experiment (Acp and Gua, n = 3 mice; Bz and Val, n = 5 mice). An additional two odors (Hex and Oca diluted at 1:100) were tested separately (Hex, n = 2 mice; Oca, n = 2 mice). The oscillation phase of each odor cycle was determined for mean traces across two trials (see **oscillation analysis** section) for glomerulus-odor pairs whose response peak was larger than 40% $\Delta F/F_0$ (Acp dataset, n = 63 and 63 pairs in m+ and m-, respectively; Gua dataset, n = 68 and 66 pairs in m+ and m-, respectively; Bz dataset, n = 60 and 55 pairs in m+ and m-, respectively; Val dataset, n = 62 and 57 pairs in m+ and m-, respectively; Hex dataset, n = 36 and 35 pairs in m+ and m-, respectively; Oca dataset, n = 36 and 29 pairs in m+ and m-, respectively). Pearson's correlation coefficient to the 1st odor cycle was calculated for this dataset.

Odor classification by phase code across sniff cycles (Figure 8C) was performed for the two pairs of odors using a Euclidean distance-based classifier. The number of glomeruli common for the two odors was n = 39 and 39 pairs in m+ and m-, respectively, for AcP and Gua; n = 38 and 33 pairs in m+ and m-, respectively, for Bz and Val. Classification between two odors was repeated with random combinations of glomeruli from the dataset (number of glomeruli, $N_{\text{glom}} = 2$ and 10); information of each odor in each cycle (10 cycles) is expressed by the phase code (oscillation phase) of N_{glom} glomeruli. The phase code in the 1st cycle was used for reference, and the remaining cycles were used as a test set. We calculated the Euclidean distance between the test condition (a vector of N_{glom} dimensions) and the reference conditions (2 vectors of N_{glom} dimensions). If the test vector is closest to a vector of the same odor, the classification was considered to be correct. The classification with $N_{\text{glom}} = 2$ was repeated for all the possible combinations of glomeruli (1056-1482 combinations) to obtain the mean correct classification rate and p values (comparison of m+ and m- using χ^2 test). The classification with $N_{\text{glom}} = 10$ was repeated until p values reached under 0.001: subsets (44-2594 combinations) of all the possible combinations of glomeruli (> 108) were used for this analysis.

Statistical tests

Statistical tests were performed using the MATLAB Statistics Toolbox. In statistical tests to assess a difference between two correlation coefficients (Figure 4F, right), correlation coefficients were converted into z-scores using Fisher's r-to-z transformation and then a two-tailed t test was performed. To compare the stability of phase code to that of rate code (Figures 5 and S5), Spearman's correlation coefficients were calculated for oscillation phase shifts ($\theta_{\text{stim}} - \theta_0$), as the counterpart rate code ($\Delta F/F_0$) represents relative changes of the activity level. To compare m+ and m- conditions (Figure 8B), correlation coefficients were calculated for oscillation phase (θ_{stim}), rather than the oscillation phase shifts ($\theta_{\text{stim}} - \theta_0$), as pre-odor oscillation phase (θ_0) could not be defined in m- conditions. The number of imaged glomeruli was determined to be sufficiently large to provide statistical power to detect differences between experimental groups. The number of odors selected to compare rate code and phase code (Figures 5, 6, S5, and S6) were at least eight to include odorants with diverse chemical structures. No blinding was performed in data analyses.

DATA AND SOFTWARE AVAILABILITY

Imaging data used in this study were deposited to Systems Science of Biological Dynamics (SSBD) database (<http://ssbd.qbic.riken.jp/set/20171001/>). Requests for the program code generated and/or analyzed during the current study should be directed to and will be fulfilled on reasonable request by the Lead Contact, Takeshi Imai (t-imai@med.kyushu-u.ac.jp).

Supplemental Information

**Mechanosensory-Based Phase Coding
of Odor Identity in the Olfactory Bulb**

Ryo Iwata, Hiroshi Kiyonari, and Takeshi Imai

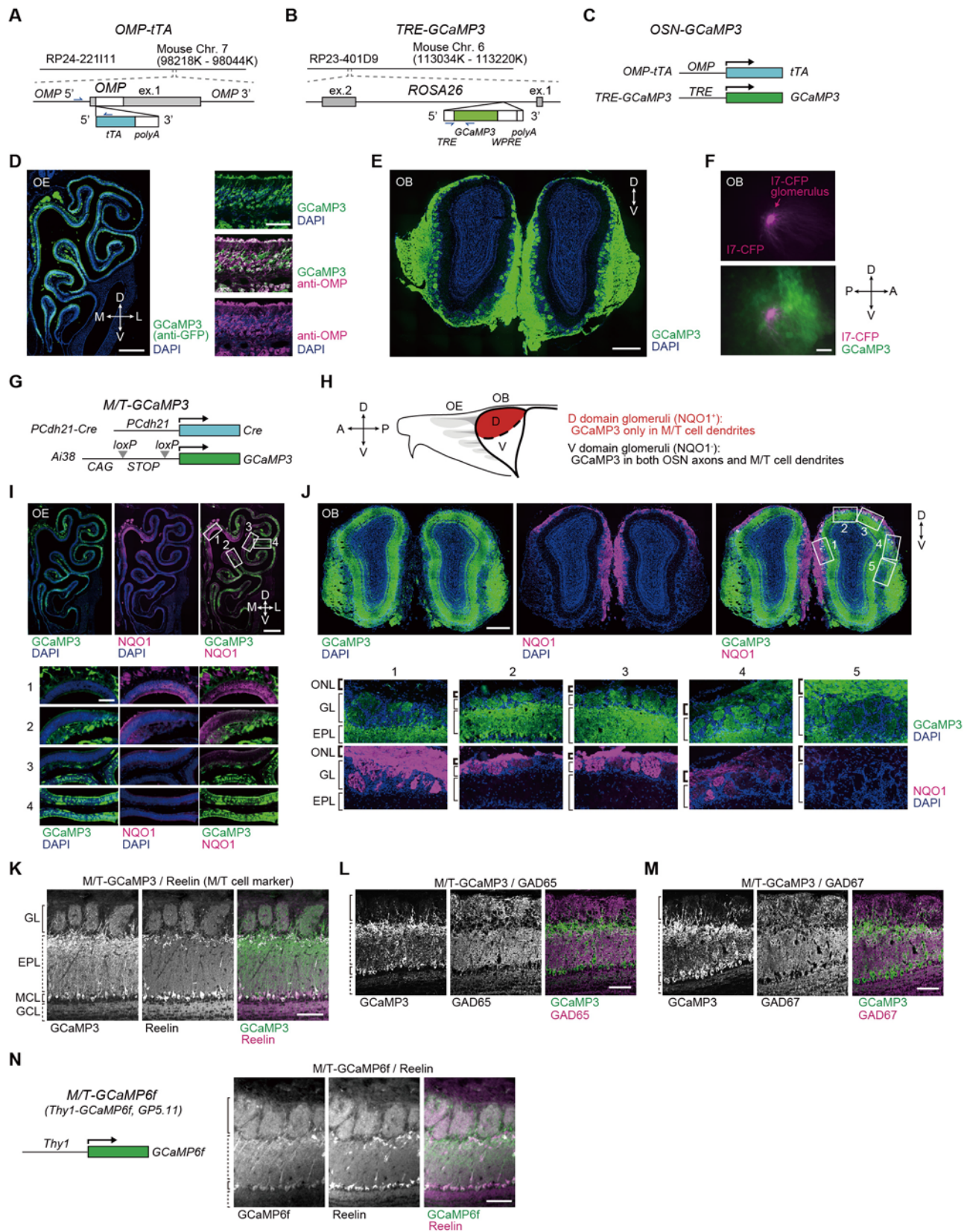


Fig S1

Figure S1. Expression of GCaMPs in *OSN-GCaMP3*, *M/T-GCaMP3* and *M/T-GCaMP6f* mice, Related to all Figures.

- (A) The BAC transgenic construct for *OMP-tTA*. The *tTA-Advanced* coding sequence was introduced into the start codon of the *OMP* in the C57BL/6J BAC clone RP24-221I11.
- (B) The BAC transgenic construct for *TRE-GCaMP3*. The *GCaMP3* coding sequence with *WPRE* under the *TRE* promoter was introduced into the *ROSA26* locus in the C57BL/6J BAC clone RP23-401D9. In (A) and (B), genotyping primer pairs are indicated by blue half arrows.
- (C) *OSN-GCaMP3* was generated by crossing *OMP-tTA* and *TRE-GCaMP3*.
- (D) A coronal section of the *OSN-GCaMP3* mouse OE stained with anti-GFP (green) and anti-OMP (magenta) antibodies. An epifluorescence image (left, scale bar 500 μ m) and higher magnification confocal images (right, scale bar 50 μ m) are shown. Expression of GCaMP3 was observed in 57.9% of OMP $^+$ cells in the OE ($n = 1881$ cells from 2 mice).
- (E) A coronal section of the OB stained with anti-GFP antibodies. Scale bar, 500 μ m.
- (F) Glomerular convergence of *I7-CFP* axons (Imai et al., 2006) (magenta) was not perturbed in the triple transgenic mouse *I7-CFP; OMP-tTA; TRE-GCaMP3* (GCaMP3, green). Scale bar, 250 μ m.
- (G) *M/T-GCaMP3* was generated by crossing *Pcdh21-Cre* (Nagai et al., 2005) and *CAG-STOP-GCaMP3* (*Ai38*) (Zariwala et al., 2012).
- (H) In the dorsal (D) domain of the *M/T-GCaMP3* mouse OB, GCaMP3 protein was expressed only in M/T cells and not in OSN axons. In the ventral (V) domain glomeruli, both OSN axons and M/T cell dendrites expressed GCaMP3. NQO1 is a marker for the dorsal zone OSNs, and the OB is divided into two domains, NQO1 $^+$ (D domain) and NQO1 $^-$ (V domain). In our two-photon Ca $^{2+}$ imaging, we only imaged the D domain of the OB.
- (I) A coronal section of the OE from *M/T-GCaMP3* mice stained with anti-GFP (green) and anti-NQO1 (magenta) antibodies. GCaMP3 expression was observed in the NQO1-negative ventral zone OSNs (images 3 and 4), but not in the NQO1-positive dorsal zone OSNs (images 1 and 2), which project axons to the D domain of the OB. This result indicates that GCaMP3 fluorescence in the D domain glomeruli was not derived from OSN axons. Scale bars, 500 μ m (left) and 100 μ m (right).
- (J) A coronal section of the OB from *M/T-GCaMP3* stained with anti-GFP (green) and anti-NQO1 (magenta) antibodies. The olfactory nerve layer (ONL) of the NQO1-positive D domain of the OB was devoid of GCaMP3 signals (bottom, images 1, 2 and 3), indicating that glomerular GCaMP3 signals in this region were not derived from OSN axons. Scale bars, 500 μ m (top) and 100 μ m (bottom).
- (K-M) Immunostaining of the *M/T-GCaMP3* OB sections with anti-Reelin (K, a marker for M/T cells), anti-GAD65 (L) and anti-GAD67 (M) antibodies. In the OB, expression of GCaMP3 was observed exclusively in M/T cells (97.8% GCaMP3 $^+$ /Reelin $^+$ cells and 100% Reelin $^+$ /GCaMP3 $^+$ cells, counted in the dorsal OB; $n = 685$ cells from 2 mice). Expression of GCaMP3 did not overlap with other interneuron markers (GAD65 and GAD67). ONL, olfactory nerve layer; GL, glomerular layer; EPL, external plexiform layer; MCL, mitral cell layer; GCL, granule cell layer. Scale bars, 100 μ m.
- (N) Immunostaining of the OB sections of *M/T-GCaMP6f* (*Thy1-GCaMP6f, GP5.11*) (Dana et al., 2014) mice with anti-Reelin. Expression of GCaMP6f was observed almost exclusively in M/T cells (79.6% of Reelin $^+$ cells were GCaMP6f $^+$, and 99.1% of GCaMP6f $^+$ cells were Reelin $^+$; $n = 401$ cells from 2 mice).

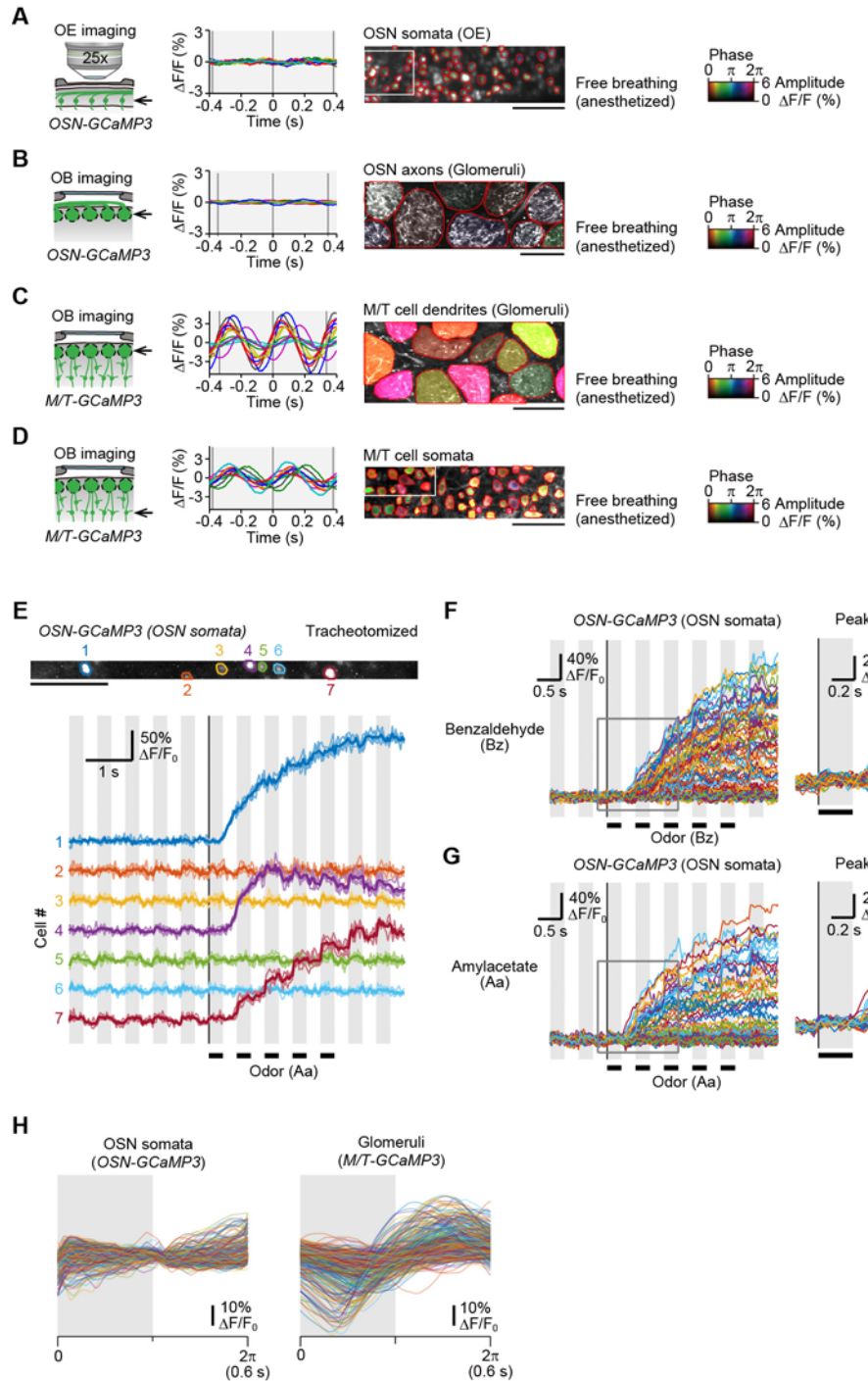


Fig S2

Figure S2. Temporal patterns of mechanosensory and odor-evoked responses in OSNs and M/T cells, Related to Figures 1, 2 and 4.

(A-D) Sniff-coupled activity from OE to OB was analyzed in freely-breathing, anesthetized *OSN-GCaMP3* or *M/T-GCaMP3* mice. Cycle-averaged activity traces during 2-min imaging sessions were obtained for OSN somata (A, shown only for cells in a boxed area), OSN axon terminals (B), M/T cell dendrites in glomeruli (C), and M/T cell somata (D, for cells in a boxed area). Gray vertical lines indicate the mean sniff cycle lengths during the imaging sessions. Half-rise phase relative to the sniff timing and oscillation amplitude are color-coded on the right.

(E-G) Odor responses in the OSN somata of tracheotomized *OSN-GCaMP3* mice. Artificial sniffing was performed at 200 ml/min and 1.67Hz. The airflow-on periods are indicated by vertical stripes in gray.

(E) Responses of seven representative OSNs to amylacetate (Aa, diluted at 1:1000). Traces in four trials and the mean traces (bold) are shown for each OSN.

(F) Left: Responses to benzaldehyde (Bz, diluted at 1:1000; n = 145 cells in n = 3 mice). Right:

A magnified view of the boxed area is shown for OSNs with peak $\Delta F/F_0 > 40\%$ (n = 51 cells).

(G) Responses to amylacetate (Aa, diluted at 1:1000; n = 111 cells in n= 3 mice) on the left and the magnified view on the right. OSNs with peak $\Delta F/F_0 > 40\%$ are shown on the right (n = 27 cells).

(H) Cycle-averaged traces from odor periods (3 s after odor onset) for OSN somata (n = 256 cells in n = 4 *OSN-GCaMP3* mice) and glomeruli (M/T cell dendrites; n = 387 glomeruli in n = 11 *M/T-GCaMP3* mice). Responses to two odorants (Aa and Bz, diluted at 1:1000) are combined. The dataset for glomeruli is from the odor experiments in Figures 4C-4E. Note that the analyses for OSN somata and glomeruli were performed under the same conditions except that cycle-averaging was performed with trial-averaged traces for OSN somata and with single-trial traces for glomeruli. Data for pre-odor periods are shown in Figure 2E.

Scale bars, 100 μ m.

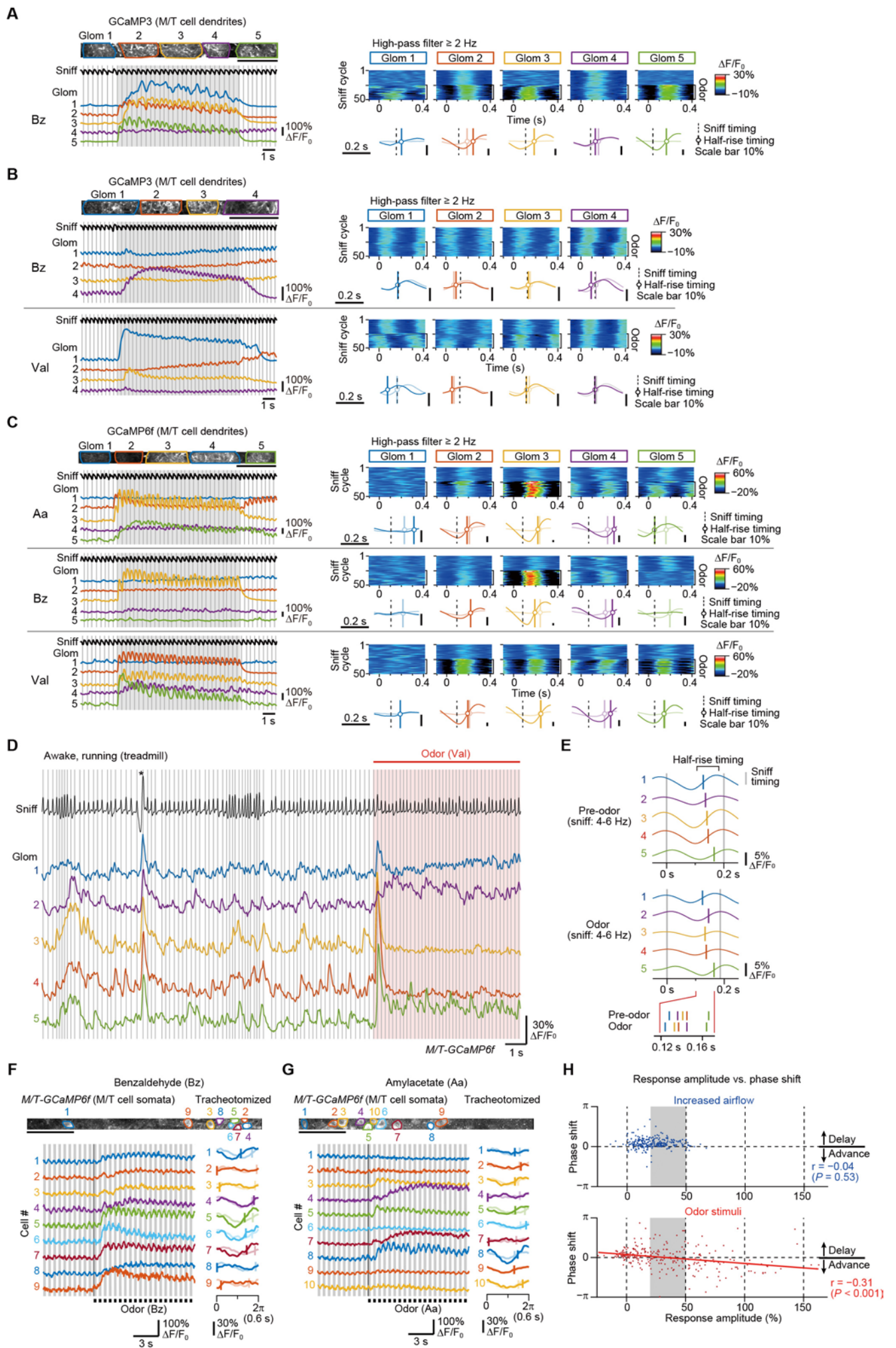


Fig S3

Figure S3. Odor-induced phase shifts in anesthetized and awake mice, Related to Figure 4.

(A and B) Phase shifts were induced by odor stimuli (diluted at 1:1000) in freely-breathing, anesthetized *M/T-GCaMP3* mice. Left: Single-trial responses and sniffing traces (vertical gray lines indicate sniff timing). Gray shaded areas indicate odor exposure periods (10 s). Right: High-pass filtered (> 2 Hz) responses aligned at inhalation onset (time = 0), showing 25 sniff cycles each before and after the stimulus onset. Mean oscillation traces were obtained by averaging 20 sniff cycles before (gray) and after (red) stimulus onset. Half-rise timing (vertical lines) is shown only for traces with detectable oscillations.

(C) The same analysis as in (A) and (B) were performed with a freely-breathing, anesthetized *M/T-GCaMP6f* mouse. In (A-C), the phase shift was glomerulus-specific: each glomerulus demonstrated unique and differential phase shifts, in both delays and advances, for the same odor. The phase shift was also odor-specific: the same glomerulus showed differential phase shifts to different odors.

(D) *In vivo* imaging of M/T cell dendrites responses to an odor (Val, valeraldehyde diluted at 1:200) in an awake *M/T-GCaMP6f* mouse running on a circular treadmill. Note that sighing (asterisk) induced large airflow responses in all the five glomeruli.

(E) Cycle-averaged traces and the half-rise timing in pre-odor and odor periods (4-6 Hz sniff frequency range). Mean sniff timing is indicated by gray vertical lines.

(F and G) Phase shifts were induced by odor stimuli (diluted at 1:1000) in M/T cell somata of tracheotomized, anesthetized *M/T-GCaMP6f* mice. Artificial sniffing was performed at 200 ml/min and 1.67Hz. Left: Single-trial responses. The airflow-on periods are indicated by vertical stripes in gray. Right: Mean oscillation traces were obtained by averaging 20 sniff cycles before (light colors) and after (dark colors) stimulus onset. The half-rise phase is indicated by vertical bars.

(H) Related to Figure 4G. Mean response amplitudes and phase shifts are only weakly correlated in odor stimuli (Pearson's correlation coefficient, $r = -0.31$) and not correlated in airflow stimuli ($r = 0.04$).

Scale bars, 100 μ m

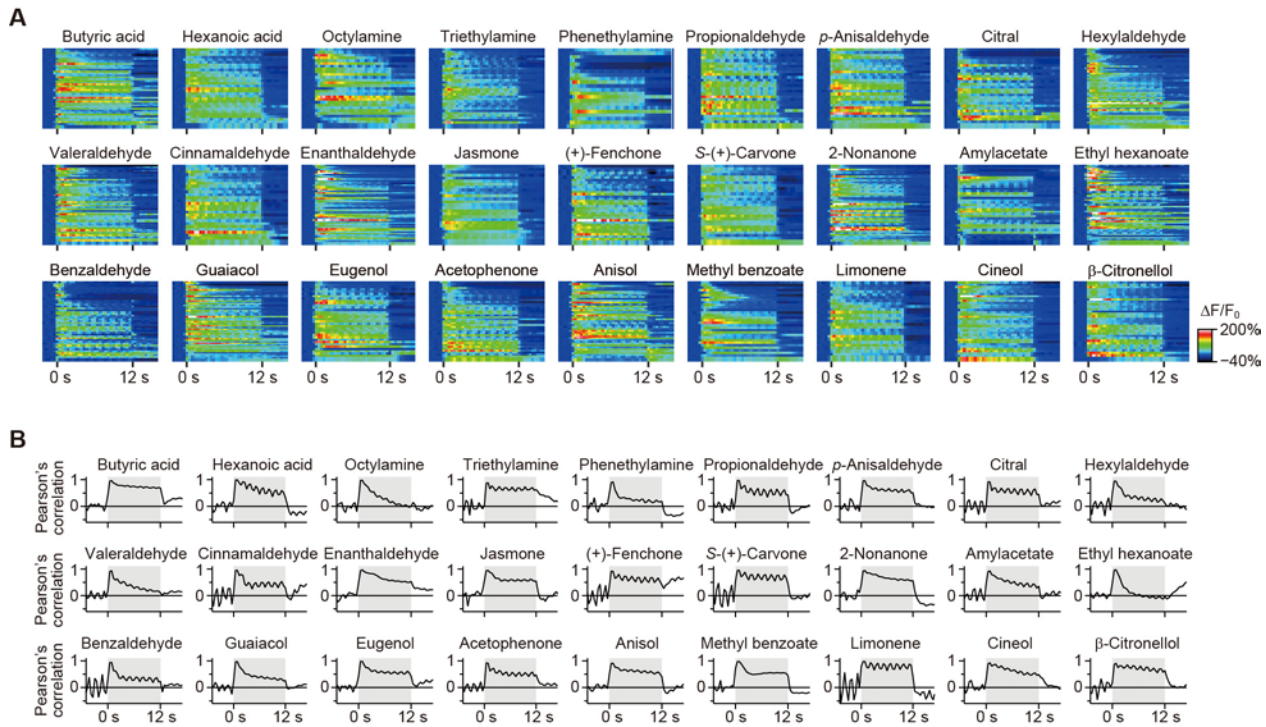


Figure S4. Temporal reorganization of the ensemble rate code, Related to Figure 5

(A) Responses to 27 odors (12 s) in tracheotomized *M/T-GCaMP3* mice (mean responses from 3 trials). Artificial sniffing was performed at 200 ml/min and 1.67Hz. Heat maps show data from $n = 22\text{-}53$ glomeruli/odor.

(B) Temporal dynamics of the ensemble rate code analyzed by correlation (Pearson's correlation coefficient). Cycle #1 was used as a reference pattern. Gray shaded areas indicate odor exposure periods (12 s). The response pattern became progressively reorganized from the initial patterns.

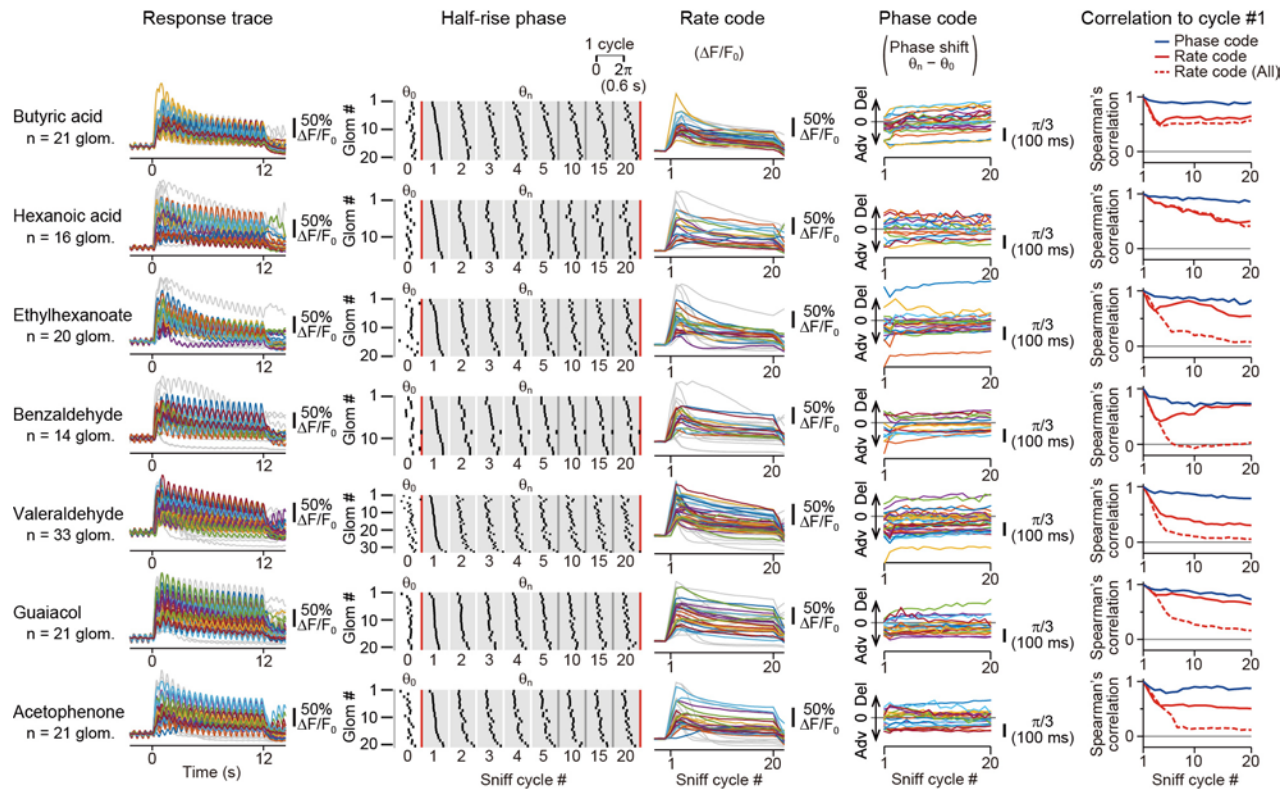


Figure S5. Phase coding is consistent across multiple sniff cycles, Related to Figure 5

Temporal reorganization of the rate code vs. phase code over 12-s odor exposure periods (20 sniff cycles) in tracheotomized *M/T-GCaMP3* mice. Artificial sniffing was performed at 200 ml/min and 1.67Hz. Response traces (left) are mean traces from 5 trials. Gray traces show the glomeruli whose oscillation phases could not be determined for all of the 20 cycles. Odor stimulation periods were 0-12 s. The second column from the left shows the oscillation phase before (θ_0) and during the odor stimulations (θ_n : n = 1-20). The third column shows the mean $\Delta F/F_0$ in each cycle (rate code). The fourth column shows oscillation phase shifts ($\theta_n - \theta_0$; phase code). In the rightmost column, the temporal dynamics of phase code and rate code were analyzed using Spearman's correlation coefficients to the reference cycle (#1). Correlation coefficients were calculated for glomeruli whose oscillation phase could be determined for all the 20 sniff cycles. The correlation of phase code and rate code are shown in blue and red, respectively. The correlation of the rate code was also determined for all the glomerular datasets (dotted red lines). See STAR METHODS for odor concentrations and sample size.

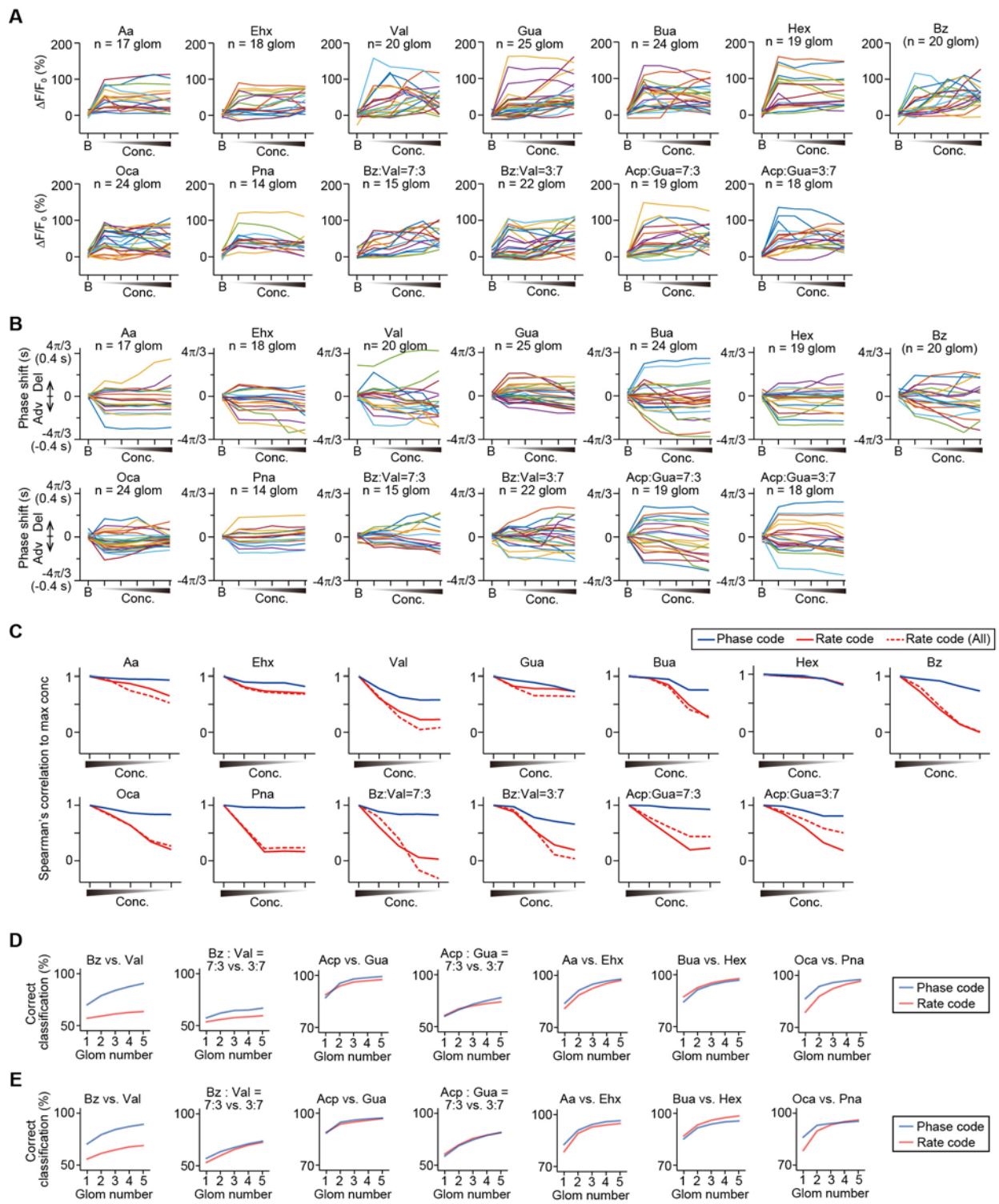


Fig S6

Figure S6. Phase code is preserved across odor concentrations, Related to Figure 6

(A and B) Concentration response curves for response amplitude (A, rate code) and oscillation phase shifts (B, phase code) in tracheotomized *M/T-GCaMP3* mice. Data are shown for blank trials (B) and odor trials (concentrations, 1:8100, 1:2700, 1:900, 1:300, and 1:100). Mean values during 6-s odor exposure periods are shown. See STAR METHODS for sample size.

(C) As in Figure 6C but for other 13 odors. Dotted red lines indicate correlation of rate code for all the glomerular dataset including glomeruli whose oscillation phase could not be determined.

(D and E) Classification between two odors by rate code (red) or phase code (blue), using an Euclidean distance-based classifier (D) and support vector machine (E), where two concentrations were randomly-chosen for each odor to classify a test odor. Chance levels are 0.5. Aa, amylacetate; Acp, acetophenone; Bua, butyric acid; Bz, benzaldehyde; Ehx, ethylhexanoate; Gua, guaiacol; Hex, hexanoic acid; Oca, octylamine; Pna, phenethylamine; Val, valeraldehyde.

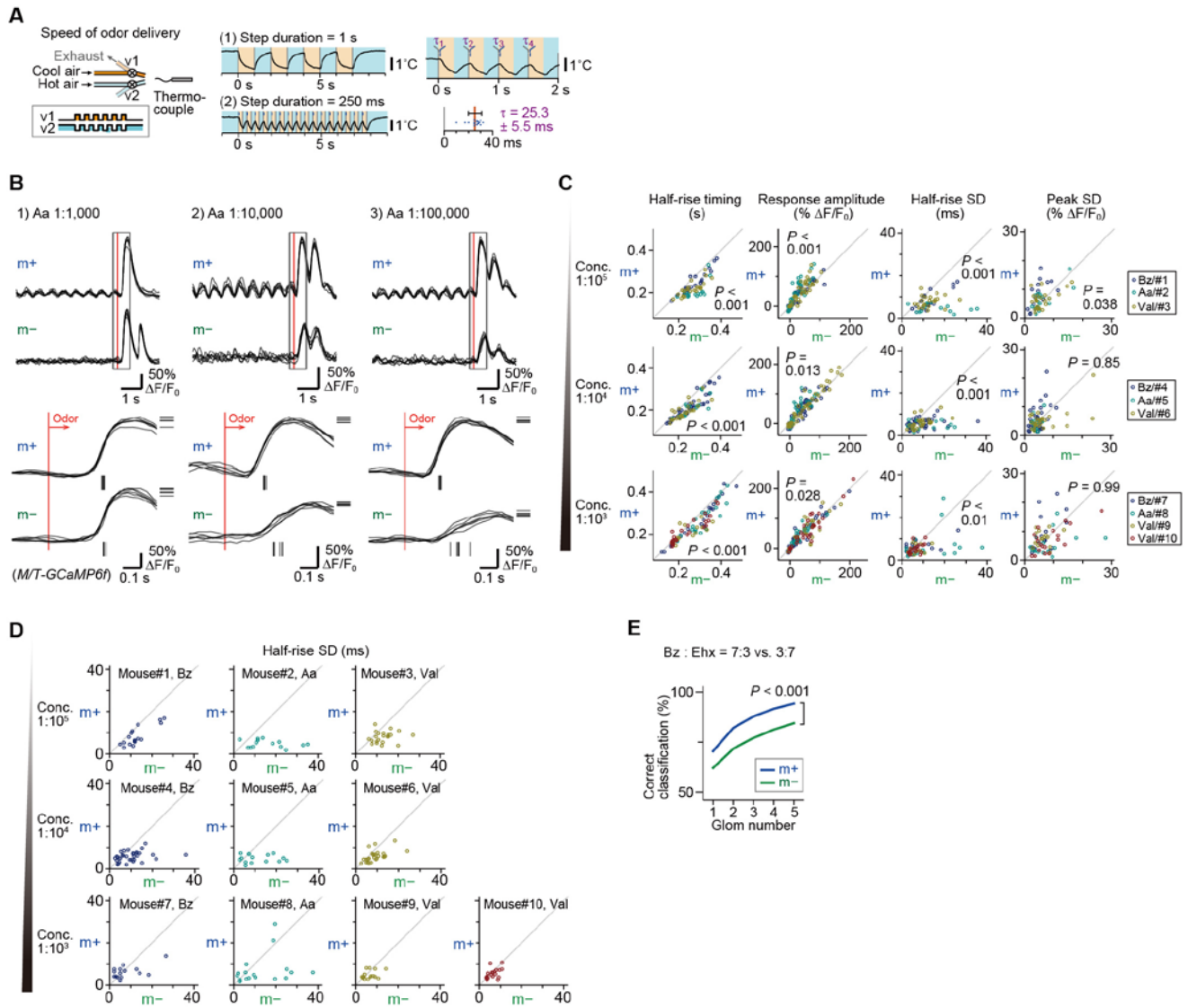


Fig S7

Figure S7. Selective elimination of mechanosensory oscillations impairs precise phase coding of odors, Related to Figure 7

(A) The air exchange rate was assessed by streaming airs of two different temperatures, which were provided alternately every (1) 1 s or (2) 250 ms. The temperature of the output air was recorded by a thermocouple. The time delay (τ) from the opening of the electrical valve to the arrival of the air (onset of monotonic decrease in temperature recordings) was 25.3 ± 5.5 ms (mean \pm s.d.) in (2), showing quick and reproducible stimulus delivery.

(B) Representative responses to odors (amylacetate diluted at 1:1,000, 1:10,000 and 1:100,000 from different glomeruli) in 6 trials each for m+ and m- conditions. Artificial sniffing was performed at 200 ml/min and 1.67Hz. Odors were applied for 1.2 s (two sniff cycles in m+). In each example, traces below are magnifications of gray boxes above.

(C) Response half-rise timing, response amplitude, half-rise SD and peak SD in m+ and m- at dilutions 1:100,000 - 1:1,000. Different colors represent different animal-odor pairs. P-values for Wilcoxon signed-rank test are indicated. Sample numbers for dilutions at 1:100,000, 1:10,000 and 1:1,000 are n = 61, 80 and 79 glomeruli for response half-rise timing; n = 114, 132 and 115 glomeruli for response amplitude; n = 56, 76 and 66 glomeruli for both half-rise SD and peak SD.

(D) Half-rise SDs plotted separately for individual mouse samples.

(E) Correct classification of two odors (mixtures of benzaldehyde and ethylhexanoate with different ratios at total concentrations 1:10,000) by a single-trial phase code (response half-rise timing) using a Euclidean distance-based classifier. Results are means of classification trials with all the possible combinations of 1-5 glomeruli from n = 19 glomeruli dataset (19-11,628 combinations). The classification success rate was significantly higher in m+ conditions ($p < 0.001$, χ^2 test). Chance levels are 0.5.

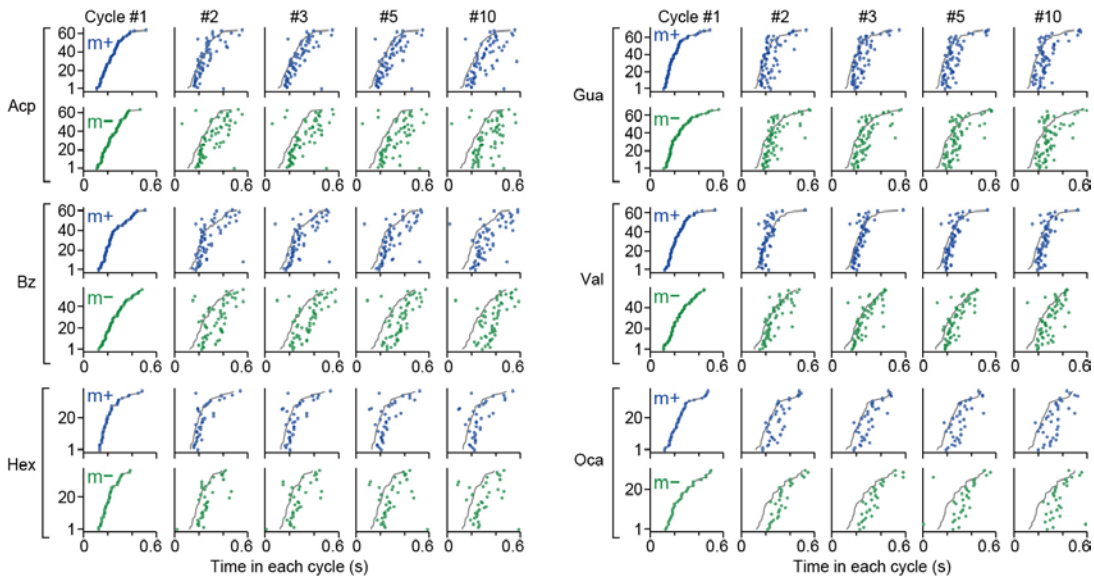


Figure S8. Phase code stability with and without mechanosensory oscillations, Related to Figure 8.

Responses to odors across 10 sniff cycles under m+ and m- conditions. Experimental configurations are shown in Figure 8A. Half-rise phase in each sniff cycle is shown for responses to acetophenone (Acp, diluted at 1:100; n = 63 glomeruli from n = 3 mice in both m+ and m-), guaiacol (Gua, diluted at 1:1000; n = 68 and 66 pairs from n = 3 mice in m+ and m-, respectively), benzaldehyde (Bz, diluted at 1:100; n = 60 and 55 pairs from n = 5 mice), valeraldehyde (Val, diluted at 1:100; n = 62 and 57 pairs from n = 5 mice), hexanoic acid (Hex, diluted at 1:100; n = 36 and 35 pairs from n = 2 mice), and octylamine (Oca, diluted at 1:100; n = 36 and 29 pairs from n = 2 mice). The half-rise phase was determined from the mean trace for two trials. Gray lines indicate the cycle #1 pattern. Correlation analysis are shown in Figure 8B and 8C.